Global properties of nuclei at finite-temperature within the covariant energy density functional theory

Ravlić, Ante; Yüksel, Esra; Nikšić, Tamara; Paar, Nils

Global properties of nuclei at finite-temperature within the covariant energy density functional theory

Ante Ravlić [*]
Facility for Rare Isotope Beams, Michigan State University, East Lansing, Michigan 48824, USA
and Department of Physics, Faculty of Science, University of Zagreb, Bijenička c. 32, 10000 Zagreb, Croatia

Esra Yüksel [†]
Department of Physics, University of Surrey, Guildford, Surrey GU2 7XH, United Kingdom

Tamara Nikšić [‡] and Nils Paar [§]
Department of Physics, Faculty of Science, University of Zagreb, Bijenička c. 32, 10000 Zagreb, Croatia

(Received 17 September 2023; revised 10 November 2023; accepted 8 December 2023; published 16 January 2024)

In stellar environments nuclei appear at finite temperatures, becoming extremely hot in core-collapse supernovae and neutron-star mergers. However, due to theoretical and computational complexity, most model calculations of nuclear properties are performed at zero temperature, while those existing at finite temperatures are limited only to selected regions of the nuclide chart. In this study we perform the global calculation of nuclear properties for even-even $8 \leqslant Z \leqslant 104$ nuclei at temperatures in range $0 \leqslant T \leqslant 2$ MeV. Calculations are based on the finite-temperature relativistic Hartree-Bogoliubov model supplemented by the Bonche-Levit-Vautherin vapor subtraction procedure. We find that near the neutron-drip line the continuum states have significant contribution already at moderate temperature $T \approx 1$ MeV, thus emphasizing the necessity of the vapor subtraction procedure. Results include neutron emission lifetimes, quadrupole deformations, neutron-skin thickness, proton and neutron pairing gaps, entropy and excitation energy. Up to the temperature $T \approx 1$ MeV, the nuclear landscape is influenced only moderately by the finite-temperature effects, mainly by reducing the pairing correlations. As the temperature increases further, the effects on nuclear structures become pronounced, reducing both the deformations and the shell effects.

DOI: 10.1103/PhysRevC.109.014318

I. INTRODUCTION

Highly excited (hot) nuclei can be described as compound nuclei, characterized only by their excitation energy E^* and angular momentum J, according to Bohr's hypothesis [1]. Such nuclei have no memory regarding their formation, and if in thermodynamical equilibrium, they decay by a slow particle or gamma evaporation, having a short lifetime of the order 10^{-22} s. The temperature T defines the statistical decay properties of a compound nucleus. One can find very hot nuclei in extreme stellar environments, such as core-collapse supernovae (CCSNe), where the temperatures exceed 2 MeV [2]. Furthermore, temperatures can be even higher in neutron-star mergers, one of the prime candidates for the r-process site [3], identified as possible source of a considerable amount of the chemical elements heavier than iron. Therefore, there is a strong motivation for studying the properties of finite nuclei at high temperatures.

Experimentally, the study of hot nuclei is a very challenging task. Primarily, nuclei at finite temperatures are studied by compound nucleus formation, either by the nuclear fusion reactions [4], studying their decay products [5], or by measuring the temperature from relative population of excited states [6,7]. Concerning the investigation of decay products, especially important is the study of excited nucleus giant dipole resonance (GDR) decay [8–13]. Considering a simple complete fusion reaction, the laboratory beam energy can be related to the nuclear masses and excitation energy E^*. A compound nucleus is formed, which then decays mostly by the emission of light particles or photons, as dictated by the density of states. Assuming a highly excited nucleus, a simple Fermi gas description of the excitation yields $E^* = aT^2$, where a is the density of states parameter [14]. The decay is described by a level density being proportional to $\exp(\sqrt{aE^*})$. Of course, such a simple model is not realized in practice since the fusion reactions are usually incomplete, complicating the kinematics of the model by introducing the residual nucleus. Furthermore, only at very high temperatures ($T \geqslant 3$ MeV) is the Fermi relation approximately valid. On the practical side, additional difficulties arise from the necessity of detecting all decayed particles. For temperature to be well defined, the compound nucleus has to be in a metastable state, i.e., thermalized, and decay has to be in equilibrium.

Theoretically, the study of hot nuclei is concerned with either static or dynamic properties. Starting from the mean-field

[*] ravlic@frib.msu.edu
[†] e.yuksel@surrey.ac.uk
[‡] tniksic@phy.hr
[§] npaar@phy.hr

picture of a nucleus, time-evolution of the density operator is achieved by solving the time-dependent finite-temperature Hartree-Fock (TDFT-HF) equations, allowing for the study of the dynamic effects, which are of importance in nuclear reactions such as heavy-ion collisions [15,16]. By solving the static FT-HF equations, one obtains the picture of a thermalized compound nucleus at finite temperature. If the temperature is high enough, the main properties of a nucleus at finite temperature can be well described by a simple semiclassical or Thomas-Fermi approximation instead of a quantum treatment [17,18]. The finite temperature is usually introduced within either canonical or grand-canonical ensemble through a noninteracting HF density matrix. In the HF basis, diagonal matrix elements correspond to the temperature dependent Fermi-Dirac distribution function. Therefore, the nucleons can scatter above the Fermi level, and temperature smears the Fermi surface. This leads to a nonvanishing number of single-particle states found in the particle continuum. A continuum state is characterized by positive single-particle energy and wave functions that do not asymptotically vanish at large distances from the nucleus. Theoretical treatment of continuum states requires special care, either by explicitly constructing the many-body Green's function in the spectral representation [19,20] or approximately within the Thomas-Fermi approximation [21]. Such methods are numerically expensive and impractical for large-scale studies of static nuclear properties. Almost 40 years ago, Bonche, Levit, and Vautherin developed a method that allows for vapor subtraction in a straightforward way [22,23]. It is based on the fact that static FT-HF equations correspond to solving a system consisting of a nucleus surrounded by its external vapor. A prescription is given on how to separate the contribution of the continuum, by subtracting the vapor from the FT-HF solution. Once the vapor is removed, the results of the main observables become independent of the basis size. Later, the subtraction procedure was also justified within the Green's function formalism [24].

The introduction of pairing correlations in the FT-HF can be realized by performing the Bogoliubov transformation of the single-particle operators, yielding the FT-HF Bogoliubov (FT-HFB) equations. Approximately, it can be also realized within the FT-HF Bardeen-Cooper-Schrieffer (FT-HFBCS) theory, where the mean-field and pairing interactions are decoupled [25]. It is well known that finite-temperature effects lower the strength of the pairing correlations, which can be expressed as reduction of pairing gaps with increasing temperature, resulting eventually in the pairing collapse at the critical temperature [25–27]. Furthermore, temperature influences the single-particle energies, leading to a shape transition from a deformed to a spherical shape. Most nuclei at $T > 3$ MeV, being highly excited, are in a normal state (no pairing correlations) and have a spherical shape [27,28]. With the advent of the nuclear energy density functional (EDF) theory, systematic calculations of finite-temperature properties across the nuclide chart have become feasible. At zero temperature, a significant amount of work has been done with the nonrelativistic EDFs such as Skyrme or Gogny within the HFB theory [29–31]. On the other hand, results at finite-temperature are somewhat more scarce, restricted to selected nuclei and observables. The investigation was performed on the temperature dependence of neutron-skin thickness [32], the evolution of pairing gaps with temperature [33,34], the influence of temperature on fission barriers [35,36], as well as clustering phenomena [37], while the Bonche-Levit-Vautherin (BLV) vapor subtraction was only considered in calculating the neutron emission lifetimes [38] and the properties of some selected nuclei [39]. Recently, a global study of finite-temperature properties has been performed across the nuclide chart within the nonrelativistic EDF, however, without treatment of the continuum [40]. The extension to relativistic EDFs is achieved through the relativistic FT-HFB theory (FT-RHFB), or the FT-RHB theory, if the Fock terms are omitted [41,42]. The starting point in defining the relativistic EDFs is the Lagrangian density in which Dirac particles (nucleons) can be written either as exchanging a set of different mesons (meson-exchange) [43] or as a sum of bilinear covariants of Dirac fields (point-coupling) [44]. The ground-state properties at zero-temperature have been thoroughly investigated across the nuclide chart by employing multiple relativistic EDFs in Refs. [45–47]. At finite temperature, pairing properties were investigated by assuming spherical nuclei within the FT-RH(F)B theory in Refs. [33,48]. Shape transitions were studied at the FT-HF mean-field level [49] and by using the FT-HBCS theory [50,51], confirming that nuclei collapse to spherical configurations above $T > 3$ MeV. In Ref. [52] multiple observables were studied by including the BLV vapor subtraction. Only recently, in Ref. [53], have the finite-temperature drip lines been thoroughly mapped within the relativistic EDF framework using a proper vapor subtraction.

The aim of this work is to conduct a global study of nuclear properties at finite temperatures for even-even $8 \leqslant Z \leqslant 104$ nuclei. Calculations are performed within the framework of the finite-temperature relativistic Hartree-Bogoliubov model supplemented by Bonche-Levit-Vautherin vapor subtraction procedure. Although the effects of the triaxial deformations can be significant at finite temperatures [50,51], computational cost of such calculations still precludes systematic large-scale calculations. Therefore, axial symmetry is assumed throughout this work.

To assess the robustness of our results, calculations are performed with three state-of-the-art relativistic EDFs: the meson-exchange DD-ME2 functional [43] and the point-coupling DD-PC1 [44] and DD-PCX functionals [54]. Throughout this work, we also compare our results with those obtained in a similar recent study based on the nonrelativistic EDFs [40]. Such comparisons should be very useful from the aspect of uncertainty quantification, since it is important to have many different calculations stemming from different theoretical models to better assess theoretical uncertainties. We notice that the present study is more complete because the calculations performed in Ref. [40], and the majority of the previous studies at finite temperature [32–34,48,50,51,55], omit the continuum contributions, which are shown to be essential for nuclei near the drip line (see Ref. [53]). Therefore, by comparing with our calculations both with and without the continuum subtraction, we can get a better understanding of the importance of the particle continuum in finite-temperature studies.

The paper is organized as follows: In Sec. II we present the FT-RHB model supplemented with the vapor subtraction procedure. The importance of the proper continuum treatment is demonstrated in Sec. III. The large-scale calculation of neutron emission lifetimes is presented in Sec. IV. Global calculations of bulk properties of even-even $8 \leqslant Z \leqslant 104$ nuclei at finite-temperature are given in Sec. V. A brief summary and outlook for future studies are presented in Sec. VI.

II. THEORETICAL FORMALISM

Nuclei at finite temperature can be treated as open systems that exchange both heat and particles described within the grand-canonical ensemble. Such a system is characterized by its grand potential Ω. To calculate the thermal properties of nuclei, we employ the relativistic EDF approach [41,42,56], described by the generalized Bogoliubov-Valatin density $\mathcal{R}$, being a statistical mixture of excited states at finite-temperature [25,57]. It assumes a form

$$\mathcal{R} = \begin{pmatrix} \rho_{kk'} & \kappa_{kk'} \\ -\kappa^*_{kk'} & 1-\rho^*_{kk'} \end{pmatrix}, \tag{1}$$

where ρ is the particle density and κ is the pairing tensor. They are defined as thermal averages $\langle\cdot\rangle_T$ of quasiparticle (q.p.) operators [25,57]

$$\rho_{kk'} = \langle \beta^\dagger_{k'}\beta_k\rangle_T, \quad \kappa_{kk'} = \langle \beta_{k'}\beta_k\rangle_T. \tag{2}$$

The set of indices (k, k') spans a $2M \times 2M$ dimensional space of Bogoliubov quasiparticles (q.p.) $(\beta_k, \beta^\dagger_k)$, M being the number of q.p. states. To account for a nonvanishing number of particles in the continuum at finite temperature, we have implemented the BLV subtraction procedure (for details about the BLV procedure, we refer the reader to Refs. [22,23]). The subtracted grand potential is introduced as

$$\bar{\Omega} = \Omega[\mathcal{R}] - \Omega[\tilde{\mathcal{R}}] + E_c[\rho_p, \tilde{\rho}_p], \tag{3}$$

where $\mathcal{R}$ indicates the generalized density of the Nucleus + Vapor system (Nuc + Vap) and $\tilde{\mathcal{R}}$ corresponds to the vapor-only system (Vap). To account for the vapor-nucleus Coulomb interaction, the BLV prescription proposes a form of the Coulomb term $E_c[\rho_p, \tilde{\rho}_p]$ which subtracts the long-range vapor contribution on the nucleus [22,23]. Here, ρ_p, $\tilde{\rho}_p$ are the proton particle densities of the Nuc + Vap and Vap systems, respectively. Variation of $\bar{\Omega}$ with $\mathcal{R}$ leads to the FT-RHB equation for the Nuc + Vap system:

$$\begin{pmatrix} h-\lambda & \Delta \\ -\Delta^* & -h^*+\lambda \end{pmatrix}\begin{pmatrix} U \\ V \end{pmatrix} = E\begin{pmatrix} U \\ V \end{pmatrix}, \tag{4}$$

where (U, V) is a set of q.p. wave functions with energy E. On the other hand, by performing variations with $\tilde{\mathcal{R}}$ we get the FT-RHB equation for the Vap system

$$\begin{pmatrix} \tilde{h}-\lambda & \tilde{\Delta} \\ -\tilde{\Delta}^* & -\tilde{h}^*+\lambda \end{pmatrix}\begin{pmatrix} \tilde{U} \\ \tilde{V} \end{pmatrix} = E\begin{pmatrix} \tilde{U} \\ \tilde{V} \end{pmatrix}, \tag{5}$$

with its corresponding set of wave functions $(\tilde{U}, \tilde{V})$ and energies $\tilde{E}$. The chemical potential λ is defined to reproduce the total particle number (either neutron or proton)

$$\int d\boldsymbol{r}[\rho(\boldsymbol{r}) - \tilde{\rho}(\boldsymbol{r})] = N. \tag{6}$$

The single-particle Dirac Hamiltonian is labeled by h, $\tilde{h}$, and the pairing field is Δ, $\tilde{\Delta}$, for the Nuc + Vap and Vap systems, respectively. The Dirac Hamiltonian can be written in terms of the scalar (S) and vector (V) potentials [58]:

$$h = -i\boldsymbol{\alpha}\nabla + \beta[m + S(\boldsymbol{r})] + V(\boldsymbol{r}), \tag{7}$$

which depend on the chosen form of the relativistic EDF, m being the bare nucleon mass. For the relativistic meson-exchange (ME) interaction, they are functions of sigma, omega, and rho-meson fields obtained by solving the corresponding Klein-Gordon equations [58]. By assuming the point-coupling functionals (PC), where meson propagators are replaced with δ functions, and the fields are expanded in terms of scalar (ρ_s), vector (ρ_v), and isovector (ρ_{tv}) densities [44]. Both interactions include a Coulomb field which satisfies the Poisson equation. The introduction of density-dependent couplings in vertices of relativistic interactions also yields a rearrangement term in vector potential [42]. In this work, we employ the density-dependent ME functional DD-ME2 [43] and two sets of density-dependent point-coupling functionals: DD-PC1 [44] and DD-PCX [54]. The difference between the Nuc + Vap Dirac field h and Vap fields $\tilde{h}$ is in the initialization of the scalar and vector fields. While for the Nuc + Vap system we assume an initial Woods-Saxon form of the potentials, the Vap system is only initialized with the Coulomb field. Due to the special treatment of the Coulomb field in Eq. (3) within the BLV prescription, the Poisson equation for the Coulomb field V_c of both Nuc + Vap and Vap systems has the form

$$-\nabla^2 V_c = e[\rho_p(\boldsymbol{r}) - \tilde{\rho}_p(\boldsymbol{r})]. \tag{8}$$

Such a term results in a coupling between the Nuc + Vap and Vap FT-RHB equations. The pairing field is calculated as

$$\Delta_{ll'} = \frac{1}{2}\sum_{kk'} V^{pp}_{ll'kk'}\kappa_{kk'}, \quad \tilde{\Delta}_{ll'} = \frac{1}{2}\sum_{kk'} V^{pp}_{ll'kk'}\tilde{\kappa}_{kk'}, \tag{9}$$

for Nuc + Vap and Vap systems, respectively. Here, V^{pp} is the matrix element of the pairing interaction for which we adopt a separable form [59]

$$V(\boldsymbol{r}_1, \boldsymbol{r}_2, \boldsymbol{r}'_1, \boldsymbol{r}'_2) = -G\delta(\boldsymbol{R} - \boldsymbol{R}')P(\boldsymbol{r}, a)P(\boldsymbol{r}', a)\tfrac{1}{2}(1 - P^\sigma), \tag{10}$$

where $\boldsymbol{R} = \frac{1}{2}(\boldsymbol{r}_1 + \boldsymbol{r}_2)$ and $\boldsymbol{r} = \boldsymbol{r}_1 - \boldsymbol{r}_2$ denote the center-of-mass and relative coordinate, respectively, while $P(\boldsymbol{r}, a) = (4\pi a^2)^{-3/2}e^{-\boldsymbol{r}^2/4a^2}$ is the Gaussian form factor. Parameters G and a describe strength and range of the pairing interaction. For DD-ME2 and DD-PC1 parametrizations we use values defined in Ref. [59], while for the DD-PCX interaction, parameters from Ref. [54] are used.

We assume axially deformed reflection-symmetric nuclei, for which the time-reversal invariance holds. This means that angular-momentum projection on the z axis Ω together with parity π is a good quantum number, with levels $\pm\Omega$ being

degenerate. The optimal configuration is obtained by performing the constrained FT-RHB calculations on the quadrupole deformation β_2, and minimizing the free energy $F = E - TS$, where E is the total binding energy and S entropy [see Eq. (21)]. We use a mesh of 11 equidistant β_2 points between $\beta_2 = -0.7$ and $\beta_2 = 0.6$. Constrained calculations are performed for the first 20 iterations, after which the constraint is lifted and calculations converge to the corresponding local minima in the (F, β_2) plane. If there are multiple local minima, the one which minimizes the total free energy is selected (global minimum). No proton-neutron mixing is assumed, allowing only for the isovector ($T = 1$) component of the pp interaction. The FT-RHB equations (4) and (5) are solved in a basis of axially deformed harmonic oscillator expanded in $N_{osc} = 20$ shells for fermion (and boson) states. We have verified that such a basis yields converged binding energies within 1 MeV for neutron-rich nuclei considered in this work. The Coulomb equation (8) is solved by direct integration using Green's function approach. Within one self-consistent iteration, the FT-RHB equations are solved twice, for the Nuc + Vap system and Vap system, supplemented with the chemical potential subsidiary condition in Eq. (6). Global calculations are performed for nuclei in the range $8 \leqslant Z \leqslant 104$. Going above $Z = 104$, we notice the existence of superdeformed minima, in agreement with results from Ref. [46]. Since our model is not suited for the treatment of those states, we perform our calculations up to the limit of $Z = 104$.

As a finite-size system, the nucleus is also influenced by fluctuations around the thermal average. Although quantal fluctuations are less relevant at finite-temperature, thermal fluctuations can play a significant role in the description of nuclei by removing the sharp transitions in pairing and deformation properties of nuclei [60,61]. If one assumes the Gaussian approximation, the thermal averages of the main observables (e.g., excitation energies, deformation, and pairing) are weighted by corresponding Boltzmann factors over many thermal configurations [62,63]. However, performing large-scale calculations by taking into account the thermal fluctuations is currently not feasible. Therefore, we did not take into account thermal fluctuations in our calculations.

III. INFLUENCE OF THE PARTICLE CONTINUUM ON THE WEAKLY BOUND NUCLEI

In this section we discuss the convergence issues that originate from the continuum contribution to the particle density once we introduce the finite temperature. If single-particle states reach the particle continuum, i.e., acquire positive single-particle energy, their energies will not converge with respect to increasing number of basis states. Already at zero temperature, one faces a similar problem, which occurs if the pairing correlations are improperly treated [64]. At finite temperature, even without pairing correlations, such a problem is more pronounced since more single-particle states get scattered across the Fermi level. Often, the contribution of particle continuum is said to be significant for nuclei at $T \geqslant 4$ MeV [17,23]. However, as we demonstrate, nuclei near the neutron drip lines show convergence problems at much lower temperatures. It is imperative to achieve proper convergence of binding energies to determine the drip lines, which are calculated from the neutron separation energies, defined as the difference between the total binding energies of neighboring nuclei.

First, we perform the axially deformed constrained FT-RHB calculation to determine the potential-energy curve (PEC) and obtain the equilibrium state (defined as the minimum of the free energy F at finite temperature). In this example, we choose two nuclei: ^{160}Gd near the stability valley and ^{210}Gd, which is predicted as a drip line nucleus by using the DD-ME2 interaction, and calculate their PECs at $T = 0$, 1, and 2 MeV. Results are presented in Figs. 1(a)–1(f) for several dimensions of oscillator basis: $N_{osc} = 20$, 24, and 28. We find that the convergence of ^{160}Gd at $T = 0$ and $T = 1$ MeV is quite satisfactory. For the prolate minimum, the difference in free energy between calculations using 20 and 28 harmonic-oscillator shells is 201 keV. This difference is somewhat higher for $T = 2$ MeV and around 514 keV. However, it is more important to note the trends. While increasing the number of shells at $T = 0$ and $T = 1$ MeV tends to improve the convergence, it actually deteriorates it for $T = 2$ MeV. Therefore, even for a nucleus near the stability valley such as ^{160}Gd, accurate evaluation of the free-energy at temperatures around $T = 2$ MeV necessitates the use of the continuum subtraction procedure. The effects of particle continuum become more pronounced for nuclei near the drip line. For ^{210}Gd at $T = 0$ MeV in Fig. 1(d), the difference in the binding energy of the predicted minimum at $\beta_2 \approx 0.35$ between 20 and 28 shells is around 50 keV. However, in Fig. 1(e) at $T = 1$ MeV, the PEC does not converge since adding four additional oscillator shells results in a decrease of energy by more than 1 MeV. The situation is even more obvious at $T = 2$ MeV in Fig. 1(f), where adding four oscillator shells shifts the position of the minimum by more than 6 MeV. Therefore, for weakly bound nuclei, we can conclude that significant problems with convergence appear already at $T = 1$ MeV, much lower than the 4 MeV stated in the literature [17,23,65].

To illustrate the impact of the continuum states, we calculate the number of states in the continuum $N_{cont.}$. To determine the single-particle energy spectrum, we perform the finite-temperature canonical transformation of the q.p. basis. Notice that, at finite temperature, canonical transformation is just an approximation since the particle density matrix is not localized [35,64]. The number of states in the continuum is defined as the number of single-particle states with positive canonical single-particle energies, $\varepsilon_i > 0$. This amounts to $N_{\text{cont.}} = 2\sum_{\varepsilon_i>0} v_i^2$, where v_i^2 denotes the occupation factor in the canonical basis. The results for neutron states of ^{210}Gd, calculated for β_2 which minimizes the free energy, are displayed in Fig. 2. Starting from zero temperature, we found approximately four neutrons in the continuum part of the energy spectrum. However, due to the specific structure of the RHB wave functions and continuum coupling, the number of states in the continuum is independent of the basis size and results converge well. Once the temperature is increased, the number of continuum states increases with the basis size. At $T = 1$

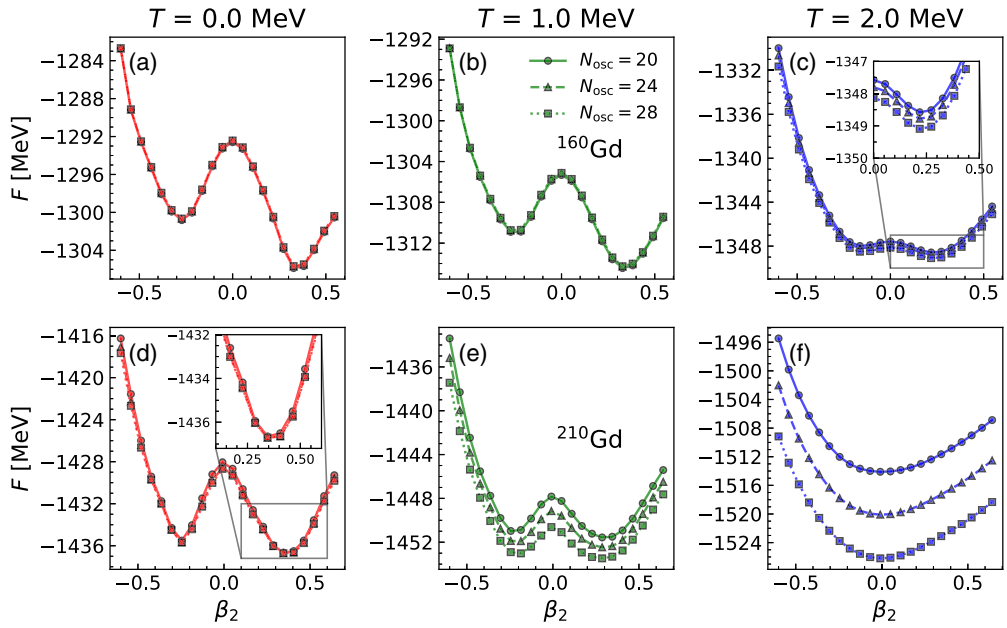

FIG. 1. Potential-energy curves (F, β_2) of (a)–(c) ^{160}Gd and (d)–(f) ^{210}Gd, calculated for $T = 0$, 1, and 2 MeV. Results are shown for different numbers N_{osc} of harmonic-oscillator shells without the BLV prescription for vapor subtraction procedure. The insets in panels (c) and (d) display enlarged regions around the corresponding minima. Calculations are performed with the DD-ME2 interaction.

MeV, the number of neutrons in the continuum increases from approximately 5.4 for $N_{osc} = 20$ shells to approximately 7.1 for $N_{osc} = 28$ shells. Of course, an increasing number of particles in the continuum contributes to the tail region of the particle density. Hence, with increasing dimension of the basis, the density tail grows and observables can display significant dependence on the basis dimension. At $T = 2$ MeV, the number of neutrons in the continuum increases significantly and depends linearly on the number of oscillator shells. The tail region of the density is now even larger and behaves as a nuclear vapor, which inflates with increasing N_{osc}. We notice that a similar behavior is found within the BCS theory in the vicinity of neutron drip lines, as demonstrated in Ref. [64]. Our results clearly show that the proper treatment of continuum is essential in the description of weakly bound nuclei nearby the drip lines, and special care must be taken at finite temperatures.

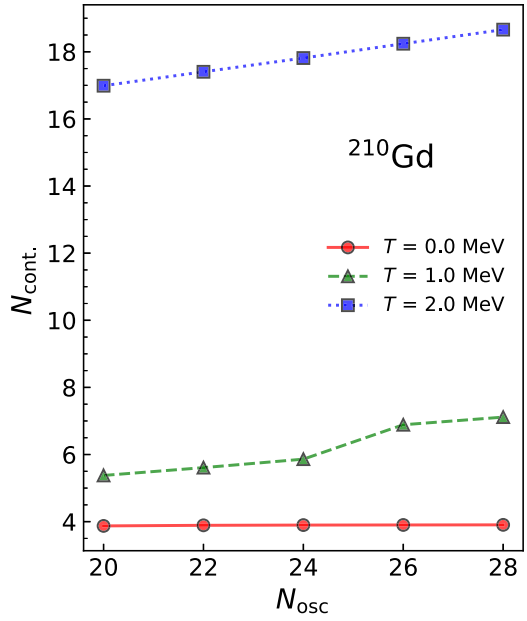

FIG. 2. Number of neutron continuum states $N_{\text{cont.}}$ in ^{210}Gd for different numbers of harmonic-oscillator shells N_{osc} at $T = 0$, 1, and 2 MeV.

Finally, the converged results can be obtained within the BLV prescription by isolating the continuum states which contribute to nucleon vapor and subtracting them from the calculated observable. In this case, the free energy F is replaced by the subtracted free energy $\bar{F}$, defined as

$$\bar{F} = F_{\text{Nuc+Vap}} - F_{\text{Vap}}, \tag{11}$$

where $F_{\text{Nuc+Vap}}$ and F_{Vap} are the free energies of the Nuc + Vap and Vap systems, respectively. Results are shown in Figs. 3(a) and 3(b), for ^{210}Gd, at $T = 1$ and 2 MeV, and converge very well with respect to the increasing size of the basis. Indeed, since the change in free energy obtained when increasing the basis size from 20 to 28 HO shells is around 100 keV, such results can be used to determine the nuclear drip lines with precision below those occurring due to systematic model uncertainties.

IV. NEUTRON EMISSION LIFETIMES

Atomic nuclei at finite-temperature are found in highly excited metastable states that can decay either by particle emission, provided that the excitation energy is above the particle-decay threshold, or by gamma emission [17]. In

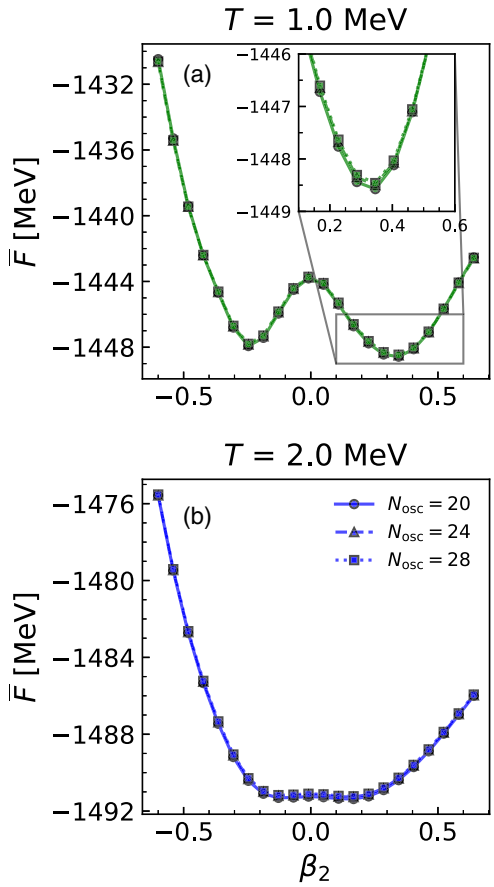

FIG. 3. (a), (b) Same as in Fig. 1, shown for ^{210}Gd at temperatures $T = 1$ and 2 MeV, but with subtracted free energy $\bar{F}$ calculated using the BLV prescription.

particular, as the temperature increases, more and more nuclei gain a finite width for neutron emission. The neutron emission width Γ_n can be obtained from the nucleosynthesis formula [23]

$$\frac{\Gamma_n}{\hbar} = n_{gas}\langle\sigma v\rangle, \tag{12}$$

where σ is the neutron capture cross section, $\langle v\rangle$ is the average velocity of particles in the external nucleon gas, and n_{gas} is the neutron vapor density calculated as number of neutrons in the vapor divided by the discretization volume. We point out that, although the number N_{Vap} of neutrons in the vapor and the discretization volume $V_{\max}$ depend on the number of shells, $n_{\rm gas}$ is independent of the basis size because it is obtained by using their ratio. However, due to the nature of HO basis functions and boundary effects, there is a small basis-dependence, which is much less significant than the temperature effects on the lifetimes. We approximate the neutron cross section as $\sigma = \pi R^2$, where the root-mean-square radius $R = (\langle r^2\rangle)^{1/2}$ of the atomic nucleus is obtained from the FT-RHB calculations. Finally, the neutron emission lifetime can be calculated as $\tau_n = \hbar/\Gamma_n$. The statistical velocity is calculated from the finite-temperature canonical single-particle neutron energies ε_n assuming the Fermi-Dirac distribution of neutrons $f(\varepsilon_n)$, therefore [38]

$$\langle v\rangle = \frac{\int_0^\infty f(\varepsilon_n)v(\varepsilon_n)\sqrt{\varepsilon_n}d\varepsilon_n}{\int_0^\infty f(\varepsilon_n)\sqrt{\varepsilon_n}d\varepsilon_n}, \quad v(\varepsilon_n) = \sqrt{\frac{2\varepsilon_n}{m_n}}, \tag{13}$$

where m_n is the neutron mass. We obtain the canonical single-particle neutron vapor states by diagonalizing the neutron vapor density $\tilde{\rho}^n$ and transforming the corresponding quasiparticle energies in this basis. This procedure is approximately valid at finite-temperature.

We present our calculations for even-even nuclei with $8 \leqslant Z \leqslant 104$. Calculations are performed with the DD-ME2 functional at $T = 1$ and 2 MeV and are displayed in Figs. 4(a) and 4(b). We choose relatively high values of temperatures because Eq. (12) is valid for highly excited nuclei. The density of states for those nuclei is described by a simple Bethe's formula [14]. Indeed, as we demonstrate later, once both pairing and deformation effects collapse [cf. Sec. V A and V C], the nucleus approximately behaves as a Fermi gas. We calculate the even-even nuclear landscape from the two-proton, up to the two-neutron drip line. The drip lines are defined as [53]

$$S_{2n} = \bar{F}(Z,N) - \bar{F}(Z,N-2) \geqslant 0, \tag{14}$$

$$S_{2p} = \bar{F}(Z,N) - \bar{F}(Z-2,N) \geqslant 0, \tag{15}$$

where S_{2n} (S_{2p}) is the two-neutron (two-proton) separation energy, and $\bar{F}(Z,N)$ the subtracted free energy of nucleus. This definition is a straightforward generalization of the zero-temperature drip line, obtained by substituting the binding energy $E(Z,N)$ with the subtracted free energy $\bar{F}(Z,N) = \bar{E}(Z,N) - T\bar{S}(Z,N)$, where $\bar{S}$ is the subtracted entropy [53]. In Fig. 4(a) we show the distribution of the neutron emission lifetimes in the nuclide map calculated at $T = 1$ MeV. All even-even nuclei between two-proton and two-neutron drip lines are included. It is interesting to notice that nuclei on the proton-rich side of the nuclide map also acquire a finite width for neutron emission at $T = 1$ MeV. Only a handful of proton-rich nuclei with $Z \leqslant 52$ are stable against neutron emission (shown as black squares). As the neutron number is increased, the neutron emission widths also increase, reducing the lifetimes by many orders of magnitude. This result is easy to explain in terms of more neutrons being scattered into the vapor states, thus increasing the neutron vapor density. At $T = 1$ MeV, pairing effects collapse, while a significant number of nuclei still display deformation properties. The shell effects are still present thus increasing the stability against neutron emission compared with neighboring nuclei. The two-neutron drip line nuclei have lifetimes of the order 10^{-21}–10^{-22} s, comparable to the nuclear thermalization timescale. By increasing the neutron number, τ_n decreases below the thermalization time, resulting in a nonequilibrated emission of nucleons [66]. To be more precise, the two-neutron drip line at finite temperature should be interpreted as a region that separates the equilibrated neutron emission from the violent multiparticle emission beyond the finite-temperature drip line. At $T = 2$ MeV in Fig. 4(b) the distribution of neutron emission lifetimes across the nuclear chart looks much smoother because the shell effects vanish at this temperature. The

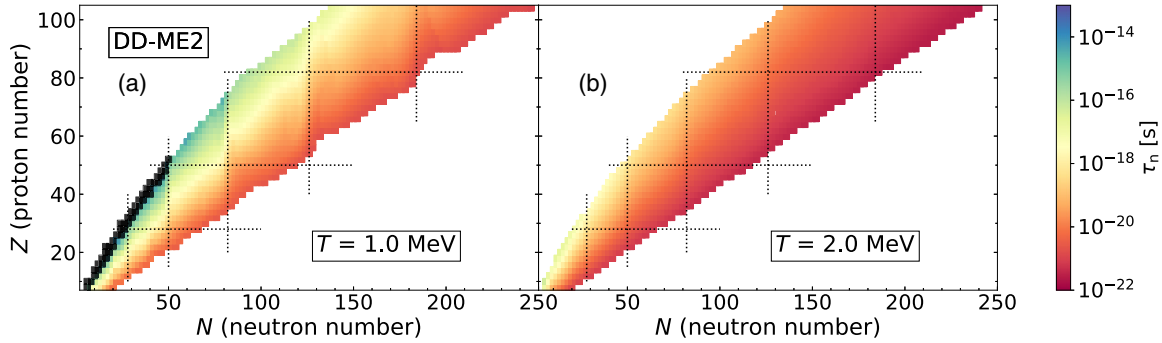

FIG. 4. Distribution of the neutron emission lifetimes τ_n for even-even nuclei with proton number in range $8 \leqslant Z \leqslant 104$ at temperatures (a) $T = 1$ MeV and (b) $T = 2$ MeV. Black dotted lines denote the shell closure numbers, while black squares represent nuclei stable with respect to neutron emission. Calculations are performed with the DD-ME2 interaction.

two-neutron drip line is approximately linear function of the neutron number, while the two-proton drip line departs from the simple linear behavior due to Coulomb repulsion. Nuclei at such high temperatures are well described by the hot liquid-drop model, requiring no shell-correction terms. Therefore, our results tend to agree with those from Refs. [18,66] above $T = 2$ MeV. The neutron lifetimes increase almost monotonically with the neutron number. However, in comparison to the calculation at $T = 1$ MeV, the average neutron emission lifetimes at the neutron drip line are closer to 10^{-22} s. We notice that, at $T = 2$ MeV, no stable nuclei exist with respect to neutron emission.

V. SELECTED BULK PROPERTIES AT FINITE TEMPERATURE

Within the BLV subtraction procedure, the mean value of an observable $\langle O[\bar{\rho}]\rangle_T$ at temperature T is a function of the subtracted density ($\bar{\rho}$), defined as the difference between the density of the Nuc + Vap system (ρ) and Vap system ($\tilde{\rho}$).

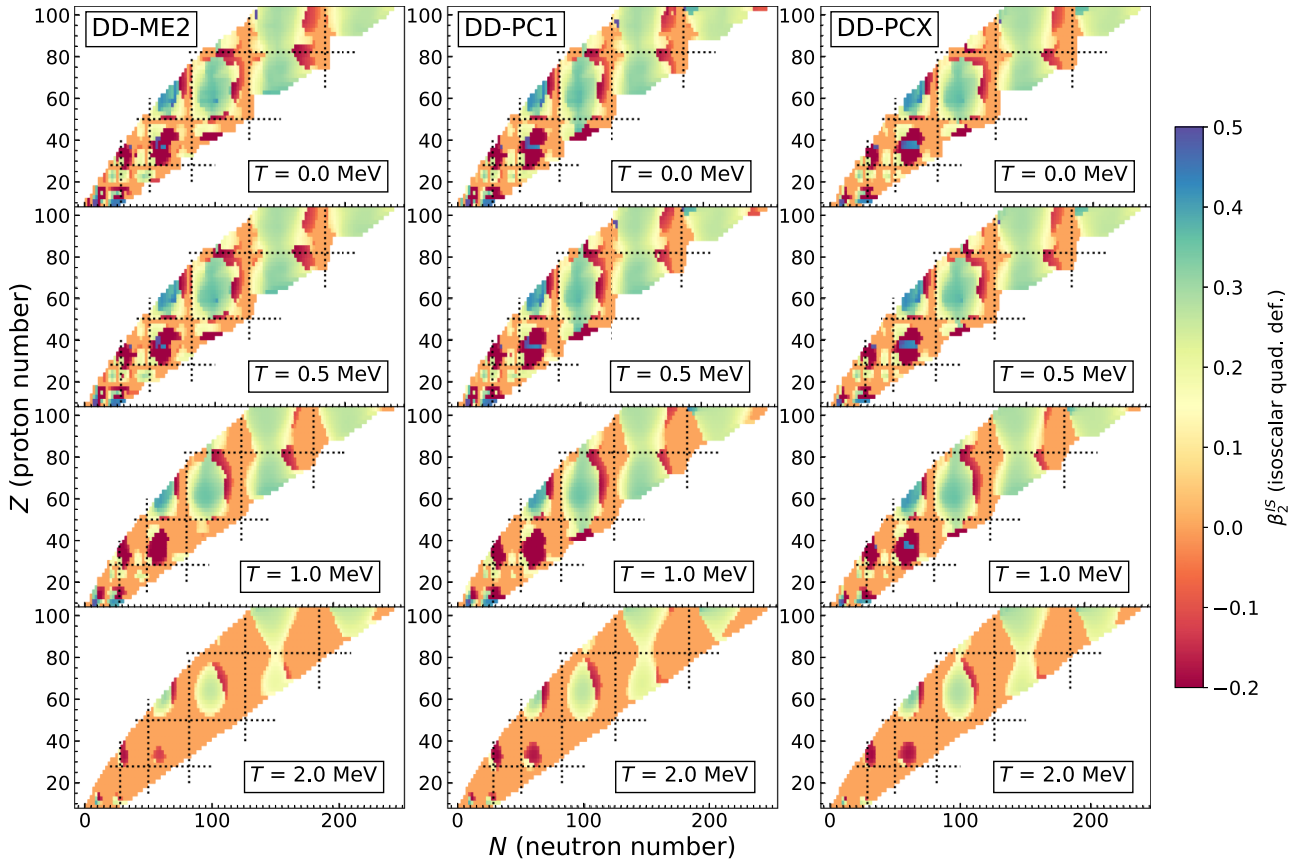

FIG. 5. Distribution of the isoscalar quadrupole deformation β_2^{IS} for even-even nuclei with proton number $8 \leqslant Z \leqslant 104$ at temperatures $T = 0$, 0.5, 1, and 2 MeV. Calculations are performed with DD-ME2 (left panels), DD-PC1 (middle panels), and DD-PCX (right panels) interactions.

For the relativistic EDFs, the baryonic density is equal to the vector density $\bar{\rho}_v$, which satisfies Eq. (6). In the following, we present the results for the temperature evolution of isoscalar quadrupole deformation, neutron-skin thickness, pairing gap, entropy, and excitation energy, for even-even $8 \leqslant Z \leqslant 104$ nuclei.

A. Quadrupole deformation

Starting from the proton (neutron) subtracted vector density $\bar{\rho}_v^p$ ($\bar{\rho}_v^n$) the proton (neutron) quadrupole moment is defined as [46]

$$Q_{20}^p = \int d^3r \bar{\rho}_v^p(\boldsymbol{r})(2z^2 - r_\perp^2),$$
$$Q_{20}^n = \int d^3r \bar{\rho}_v^n(\boldsymbol{r})(2z^2 - r_\perp^2), \tag{16}$$

where $(r_\perp, z)$ are the cylindrical coordinates. It is more customary to express the results in terms of dimensionless variable β_2^p (β_2^n) defined as

$$\beta_2^p = \frac{1}{2}\sqrt{\frac{5}{4\pi}}\frac{3}{4\pi}Z(N)R_0^2Q_{20}^p, \tag{17}$$

$$\beta_2^n = \frac{1}{2}\sqrt{\frac{5}{4\pi}}\frac{3}{4\pi}Z(N)R_0^2Q_{20}^n, \tag{18}$$

where $Z(N)$ denotes the proton (neutron) number and $R_0 = 1.2A^{1/3}$ fm. The isoscalar quadrupole deformation is defined as $\beta_2^{IS} = \beta_2^p + \beta_2^n$. In Fig. 5, we show the distribution of the isoscalar quadrupole deformation β_2^{IS} across the chart of nuclides for three relativistic EDFs employed in this work: DD-ME2, DD-PC1 and DD-PCX. Calculations are performed at temperatures $T = 0$, 0.5, 1, and 2 MeV. At $T = 0$ MeV we observe spherical shapes in the vicinity of closed shells and deformed for midshell nuclei. Temperature effects at $T = 0.5$ MeV are too small to alter the shell structure and deformation remains almost unchanged. At $T = 1$ MeV, we observe significant increase in number of spherical nuclei and by increasing the temperature further ($T = 2$ MeV) most nuclei display spherical shapes except those nuclei with large deformation at $T = 0$ MeV. Apart from small differences mainly for light nuclei, all employed functionals predict similar isoscalar deformations for all temperatures.

To study sudden changes in nuclear shape from $T = 1$ MeV to $T = 2$ MeV, in Figs. 6(a)–6(e) we show the distribution of β_2^{IS} across the chart of nuclides on a more refined temperature mesh: $T = 1.0$, 1.2, 1.5, 1.8, and 2.0 MeV. Calculations were performed by using the DD-ME2 interaction, but we notice that both DD-PC1 and DD-PCX interactions follow the similar behavior. The change of nuclear shapes is only moderate up to $T = 1$ MeV. However, by further increasing the temperature, it is clearly observed how the islands of axial-deformation gradually reduce in between the shell closure numbers.

To investigate the mechanism behind the temperature evolution of quadrupole deformation, we show the PEC for ^{150}Nd in Fig. 7(a), together with deeply bound single-particle canonical states shown in Fig. 7(b). The subtracted free energy

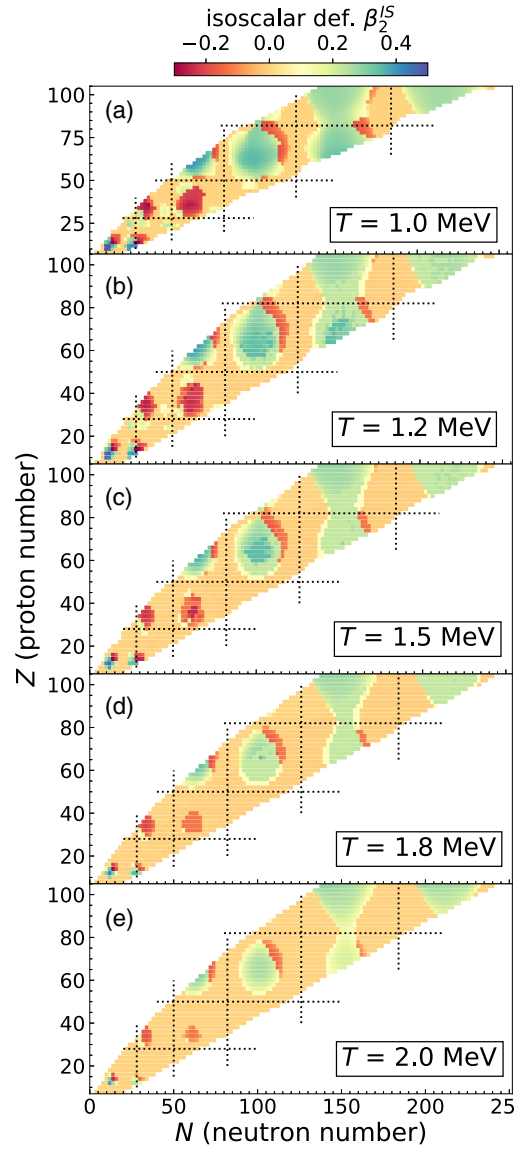

FIG. 6. Distribution of the isoscalar quadrupole deformation β_2^{IS} for even-even nuclei with proton number $8 \leqslant Z \leqslant 104$ on a more refined temperature mesh $T = 1.0$, 1.2, 1.5, 1.8, and 2.0 MeV. Results are shown for the DD-ME2 interaction.

in Fig. 7(a) is calculated relative to the global minimum at that temperature and denoted as $\Delta\bar{F}$. Calculations are again performed with the DD-ME2 interaction. At $T = 0$ MeV, the PEC for ^{150}Nd displays minima at oblate sides (located at $\beta_2 = -0.22$) and prolate sides (located at $\beta_2 = 0.29$), with the latter being the global minimum. We note that the spherical configuration ($\beta_2 = 0$) is located approximately 6 MeV above the global minimum. At $T = 1$ MeV, both prolate and oblate minima are found closer to the spherical configuration. The oblate minimum is located at $\beta_2 = -0.17$ and the prolate minimum at $\beta_2 = 0.23$. The excitation energy for the spherical shape decreases by around 3 MeV. By further increasing the temperature, at $T = 2$ MeV, the PEC displays a flat region around $\beta_2 = 0$, which is a signature of the phase transition. Finally, at $T = 3$ MeV, the minimum is at spherical shape.

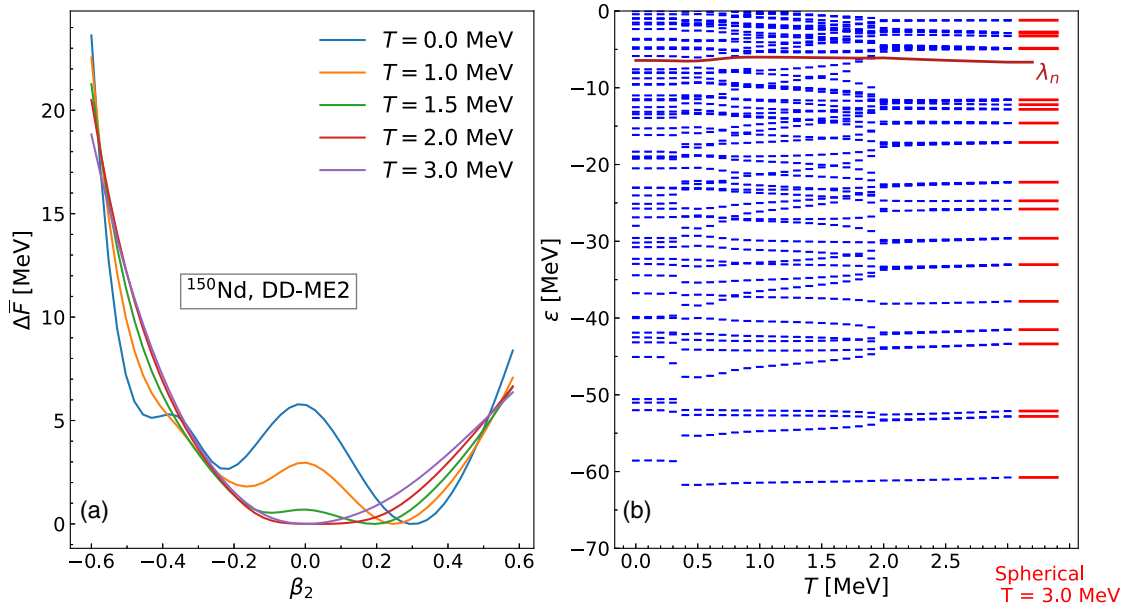

FIG. 7. (a) Potential-energy curves of ^{150}Nd isotope for temperatures in range $T = 0$–3 MeV calculated with the DD-ME2 interaction. The $\Delta\bar{F}$ represents the relative subtracted free energy with respect to the minimum energy. (b) The neutron single-particle canonical Nuc + Vap states of ^{150}Nd isotope at temperatures $T = 0$–3 MeV (blue lines) together with the corresponding spherical states at $T = 3$ MeV (red line). The neutron chemical potential λ_n is indicated by a solid brown line.

The occurrence of phase shape transitions with increasing temperature can be explained as follows: at finite temperatures, the nucleus gains approximately $k_B T$ additional excitation energy from the environment, and the population of the single-particle levels changes around the Fermi level. At high temperatures, the shell effects disappear, and with the depopulation of the intruder states, which drive the deformation, nuclei become spherical at higher excitation energies [50,67–69].

To study the signature of the phase-transition at the microscopic level, in Fig. 7(b), we also display the neutron single-particle canonical levels of the configuration that minimizes the free energy for temperatures up to $T = 3$ MeV, starting from zero temperature with a step of 0.1 MeV. Canonical single-particle levels up to the continuum threshold ($\varepsilon < 0$) are shown in the figure. The canonical single-particle states are characterized by the projection of the total angular momentum on the z axis Ω and parity π. Although only an approximation at finite temperatures, the canonical single-particle states suffice to visualize the mechanisms that drive the nucleus to spherical configuration. Starting from low temperatures up to $T = 0.5$ MeV, we observe that states corresponding to the same angular momentum J are broken into multiple states represented by the angular momentum projection Ω and parity π. The effect of the pairing collapse around $T = 0.5$ MeV clearly leaves a signature on the single-particle levels. As the temperature increases, the energy splitting between these states becomes reduced, finally resulting in restored degeneracy at around $T = 2$ MeV. In the last column in Fig. 7(b), we also show the energy spectrum at $T = 3$ MeV as calculated by imposing the spherical symmetry (red lines). We notice a perfect match between the spherical and axially deformed calculations at $T = 3$ MeV. Therefore, we anticipate a shape phase-transition in ^{150}Nd at temperatures around 3 MeV.

B. Neutron-skin thickness

The neutron-skin thickness, defined as the difference between the neutron and proton root-mean-square (rms) radii,

$$\Delta R_{np} = \sqrt{\langle R_n^2 \rangle} - \sqrt{\langle R_p^2 \rangle}, \tag{19}$$

provides a direct measure of the isospin asymmetry of the system and is related to the isovector properties of the nuclear matter [70–72]. The neutron (proton) rms radius is calculated as $\langle R_n^2 \rangle = \int_0^\infty d^3\boldsymbol{r} r^2 \bar{\rho}_v^n(\boldsymbol{r})$ [$\langle R_p^2 \rangle = \int_0^\infty d^3\boldsymbol{r} r^2 \bar{\rho}_v^p(\boldsymbol{r})$], where $\bar{\rho}_v^n$ ($\bar{\rho}_v^p$) denotes the subtracted neutron (proton) vector density.

For nuclei in the vicinity of drip-lines, it is important to properly treat the continuum contribution with increasing temperature. This is especially pronounced for neutron states since there is no Coulomb repulsion to provide a potential barrier for continuum states. Without the vapor subtraction, one would get artificially increasing neutron radii when approaching the drip-line.

The distribution of the neutron-skin thickness across the nuclide map, calculated at $T = 0$, 0.5, 1, and 2 MeV, is shown in Fig. 8 for three functionals considered in this work: DD-ME2, DD-PC1, and DD-PCX. First, we observe that the scale is skewed towards positive ΔR_{np} on the neutron-rich side compared with the negative ΔR_{np} on the proton-rich side. This is simply a consequence of the Coulomb repulsion between the protons. Results obtained for the DD-ME2 and DD-PC1 functionals are almost consistent, while the DD-PCX predicts lower ΔR_{np} for nuclei near the neutron drip-line. Such an outcome is related to different isovector properties among the

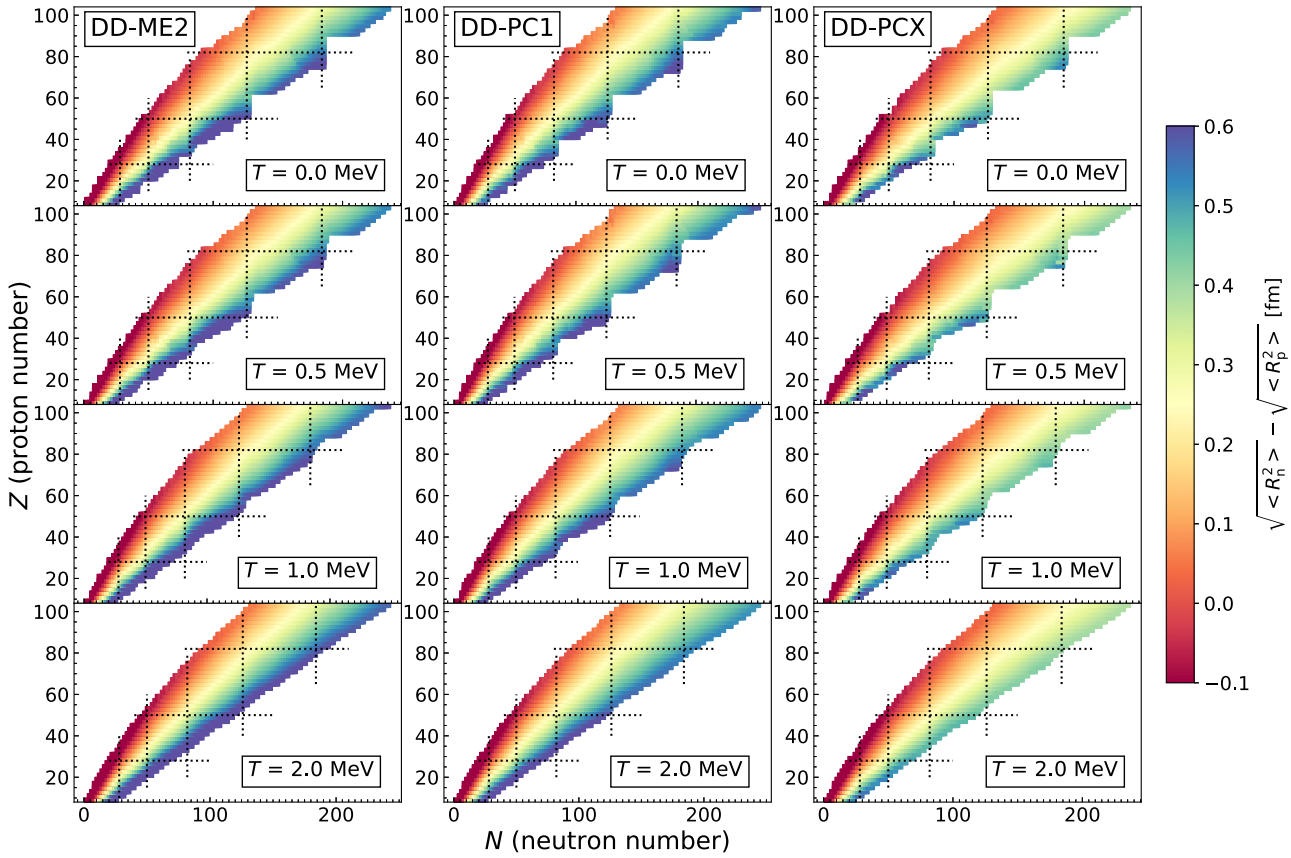

FIG. 8. Same as in Fig. 5, but for the neutron-skin thickness, defined as the difference between the neutron and proton root-mean-square radii.

functionals. It is well established that ΔR_{np} shows a linear dependence on the symmetry energy (J) and its slope (L) at saturation density, which is the smallest for DD-PCX. Such a trend is maintained for all temperatures up to $T = 2$ MeV.

To better infer the finite-temperature effects on the neutron skin, in Fig. 9, we display the temperature dependence of the neutron-skin thickness for $Z = 20$, 60, and 82 isotopic chains, calculated with the DD-ME2 interaction. We notice that, for $T = 0$, 0.5, and 1 MeV, the neutron-skin thickness is slightly influenced by the temperature. Only at $T = 2$ MeV, for $Z = 60$ and 82 chains do we observe a more pronounced departure from zero-temperature results, especially for larger neutron numbers. This is a consequence of the shape phase-transition which occurs at $T \approx 2$ MeV. Starting from the calcium chain ($Z = 20$) in Fig. 9(a) for $T \leqslant 1$ MeV, the shell effects are clearly visible in ΔR_{np} isotopic dependence, especially around $N = 28$ and $N = 40$, for which our calculations predict pairing collapse. However, as the temperature is increased, the pairing effects are washed out and isotopic dependence of ΔR_{np} becomes smoother. At $T = 2$ MeV all calcium isotopes are in a normal state (no pairing correlations) with spherical shape. This leads to linear dependence of ΔR_{np}

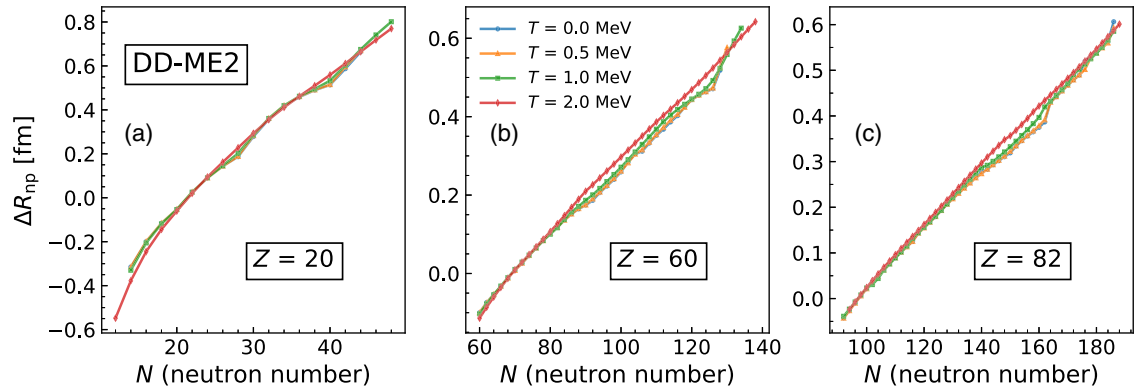

FIG. 9. The neutron-skin thickness ΔR_{np} as a function of the neutron number for (a) $Z = 20$, (b) $Z = 60$, and (c) $Z = 82$ isotopic chains at temperatures $T = 0$, 0.5, 1.0, and 2.0 MeV. Calculations are performed with the DD-ME2 interaction.

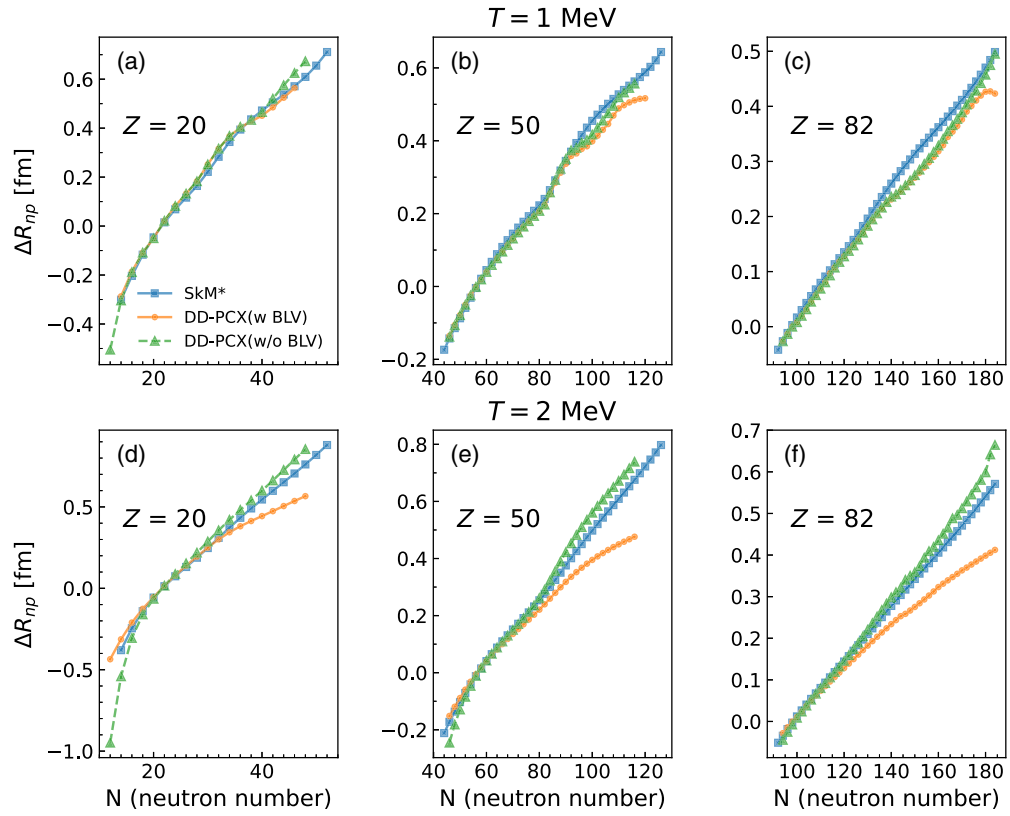

FIG. 10. The neutron-skin thickness ΔR_{np} for $Z = 20$, 50, and 82 isotopic chains at (a)–(c) $T = 1$ and (d)–(f) $T = 2$ MeV. Calculations are performed with the DD-PCX interaction both with (orange circles) and without BLV subtraction (green triangles). Also shown are the results from Ref. [40] based on the nonrelativistic SkM* interaction (blue boxes).

on neutron number. The deviations from a linear trend for $N < 20$ are due to the Coulomb effects. For the neodymium chain [see Fig. 9(b)], up to $N \approx 82$ the neutron-skin thickness is almost temperature independent. For $N > 82$ one can observe temperature effects starting already at $T = 1$ MeV. These nuclei display strongly deformed prolate minima at zero temperature. As the temperature is increased, their shape changes from prolate deformed to spherical thus causing an almost linear dependence of ΔR_{np} on neutron number for $T = 2$ MeV. We notice that, on average, the neutron-skin thickness at $T = 2$ MeV is increased compared with lower temperatures, as one would expect. Finite-temperature effects smear the Fermi surface, which leads to the occupation of higher-energy single-particle states, spreading the density tail. Similar trends are also observed for the lead chain in Fig. 9(c). We notice that in the region between $N = 130$ and $N = 160$, where ΔR_{np} is not a linear function of N, nuclei display prolate shape (see Fig. 5). As the deformation effects are washed out at $T = 2$ MeV, ΔR_{np} attains linear dependence on N. To conclude our analysis of temperature dependence of neutron-skin thickness, increasing the temperature suppresses the shell effects, thus causing a linear dependence of ΔR_{np} on neutron number N. On average, for neutron-rich nuclei ΔR_{np} increases with temperature, but only moderately. Our results are also in agreement with the findings in Ref. [52], in which proton and neutron radii stay almost constant up to $T = 2$ MeV. Considering the strong correlation between the neutron-skin thickness and the slope of the symmetry energy L, such a result indicates the stability of the L for temperatures up to $T = 2$ MeV, as remarked in Refs. [55,73].

Finally, in Fig. 10, we show a comparison of our results with those from Ref. [40] for the isotopic chains of calcium ($Z = 20$), tin ($Z = 50$), and lead ($Z = 82$). Since the nonrelativistic calculations in Ref. [40] were performed without the continuum subtraction procedure, we display results obtained with the DD-PCX interaction both with and without the BLV subtraction procedure for a fair comparison. We notice an overall good agreement between all three calculations for nuclei close to stability at $T = 1$ MeV [see Figs. 10(a)–10(c)], and some differences are observed only for neutron-rich isotopes towards the neutron drip-line. However, at $T = 2$ MeV [see Figs. 10(e) and 10(f)], the continuum contribution becomes much more pronounced. Both relativistic and nonrelativistic calculations without the continuum subtraction provide consistent results for the neutron skins that follow an almost linear trend with neutron number. On the contrary, calculations with the continuum subtraction display a clear departure from the linear trend for moderately neutron-rich isotopes. Therefore, in order to obtain an accurate description of the neutron skin at finite temperature, the continuum subtraction has to be implemented even at temperatures around $T = 2$ MeV.

C. Pairing gaps

One possible measure of the pairing correlations strength is the neutron (proton) pairing gap $\Delta_{n(p)}$. Although they can

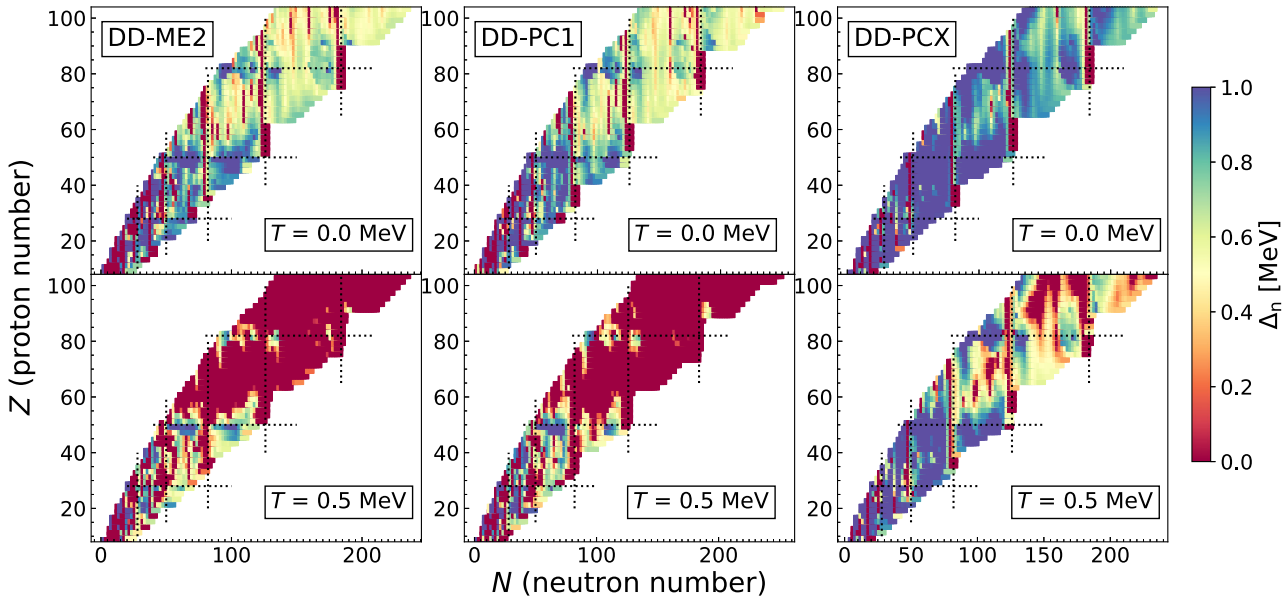

FIG. 11. Distribution of the neutron pairing gap Δ_n for even-even nuclei with proton number in range $8 \leqslant Z \leqslant 104$ at temperatures $T = 0$ and 0.5 MeV. Calculations are performed with DD-ME2 (left panels), DD-PC1 (middle panels), and DD-PCX (right panels) interactions.

be defined in multiple ways [46], in this work we employ the definition containing the pairing tensor κ[1]

$$\Delta_{n(p)} = \frac{\sum_{ik} \kappa_{ik} \Delta_{ik}}{\sum_k \kappa_{kk}}, \tag{20}$$

where Δ_{ik} is the pairing field. Both the pairing field and the pairing tensor are defined in Refs. [25,33].

The influence of the finite-temperature on the pairing properties for both relativistic and nonrelativistic functionals has been thoroughly investigated in Refs. [25,32,33,49] and therefore we keep our discussions here brief. The main result is that, with increasing temperature, one reaches a critical temperature where a phase transition occurs from the superfluid to a normal state. More complex multireference calculations as well as the ensemble averaging procedures lead to nonvanishing (although small) pairing gaps [62,63]. In this study, we omit thermal averaging because it would be computationally prohibitive for large-scale calculation. For all three functionals employed here (DD-ME2, DD-PC1 and DD-PCX), we use the same separable form of the pairing interaction defined in Refs. [33,59]. For both DD-ME2 and DD-PC1 functionals, we use the original values of the pairing interaction parameters G and a, while for the DD-PCX functional these parameters have been included in the optimization procedure [54]. As a result, the pairing strength parameters of the DD-PCX interaction are around 10% larger compared with the DD-ME2 and DD-PC1.

The distribution of neutron and proton pairing gaps $\Delta_{n(p)}$ across the nuclide map is shown for all three functionals in Figs. 11 and 12. Calculations are performed for temperatures $T = 0$ and 0.5 MeV. We observe that both the neutron and proton pairing gaps vanish in the vicinity of closed shells and increase towards the midshell nuclei. On average, the proton pairing gaps are larger in comparison with the neutron pairing gaps. Due to the similar pairing strength, results for DD-ME2 and DD-PC1 functionals are comparable, while the DD-PCX predicts significantly larger pairing gaps. As the temperature increases to $T = 0.5$ MeV, the neutron pairing gaps vanish in a considerable number of nuclei for DD-ME2 and DD-PC1 functionals, while the results calculated with the DD-PCX show a moderate decrease of the neutron pairing gaps with temperature. Further increasing the temperature to $T = 1$ MeV results in neutron pairing collapse for all considered functionals. The proton pairing gaps also decrease when the temperature increases to $T = 0.5$ MeV, but not as dramatically as the neutron ones. Again, the DD-PCX shows the least change with temperature due to the higher proton pairing strength. By increasing the temperature to $T = 1$ MeV, only very light nuclei ($Z < 20$) display nonvanishing proton pairing correlations. Therefore, we can conclude that for the vast majority of atomic nuclei, only deformation effects are relevant above $T = 1$ MeV, for both proton and neutron states.

D. Entropy and excitation energy

Unlike the bulk properties discussed in the previous section, entropy is not an observable in the sense that it could be obtained from experiments. Nevertheless, it can provide us with further guidance in interpreting our theoretical calculations. The entropy is a direct measure of occupancy of single-(quasi)particle orbitals and strongly correlates with the underlying microscopic structure. It is defined as [25]

$$S = -k_B \sum_i [f_i \ln f_i + (1 - f_i) \ln(1 - f_i)], \tag{21}$$

where $f_i = [1 + \exp(\beta E_i)]^{-1}$ is the Fermi-Dirac factor for q.p. state with energy E_i, and $\beta = 1/k_B T$.

In Figs. 13(a)–13(c), we show the entropy as a function of neutron number for selected isotopic chains $Z = 20$, $Z = 60$,

[1]Within the BLV prescription we use the subtracted pairing tensor $\bar{\kappa}$, but since the vapor contribution to pairing is negligible, $\kappa \approx \bar{\kappa}$.

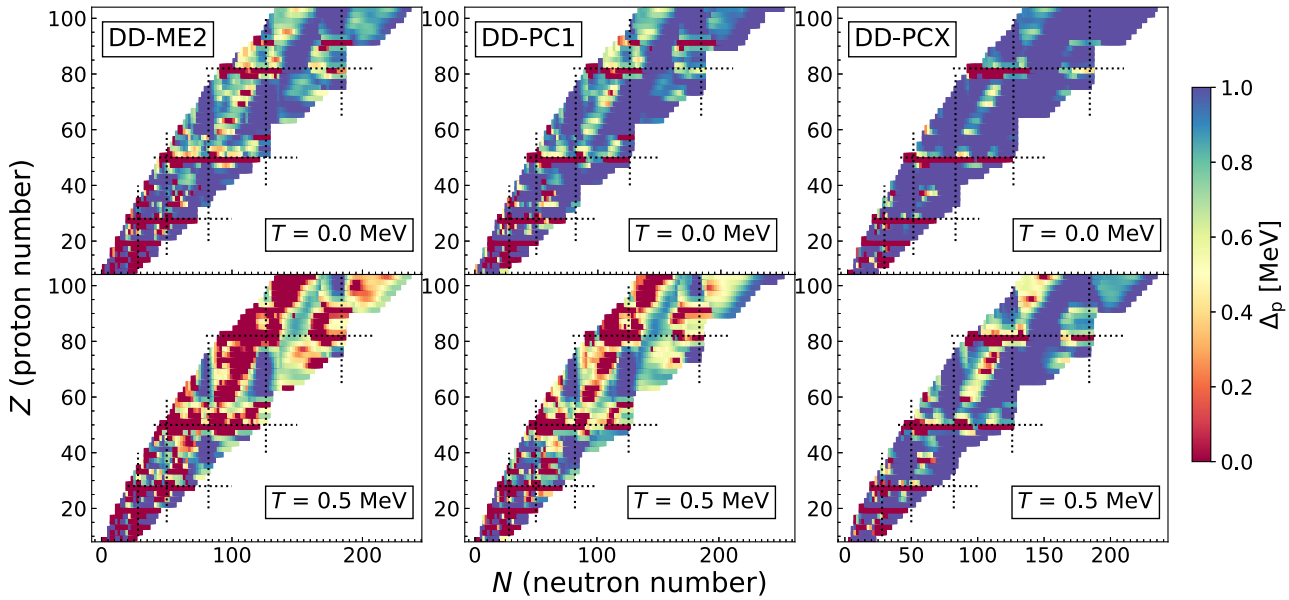

FIG. 12. Same as in Fig. 11 but for the proton pairing gaps Δ_p.

and $Z = 100$, calculated at $T = 0.5$, 1, and 2 MeV. Full and dotted lines denote calculations assuming axial and spherical symmetry, respectively. Starting from the calcium isotopic chain in Fig. 13(a) at $T = 0.5$ MeV, we observe that the entropy has highly irregular isotopic dependence. Dips observed for $N = 20$, 28, and 40 correspond to the neutron shell closures. From the definition of entropy in Eq. (21), it can be inferred that only those levels with semi-occupied shells around the Fermi level contribute to entropy. For closed shells, all levels are almost fully occupied and only slightly smeared around the Fermi level due to the finite-temperature effects. Therefore, closed shells will be represented as dips when studying the isotopic entropy dependence. As one moves away from closed shells towards the midshell, the number of neither completely empty nor completely occupied states increases, resulting in entropy increasing as well. Also shown are the results assuming spherical symmetry (dotted lines). For the calcium isotopic chain, results between spherical and axially symmetric calculations agree up to the two-neutron drip line. At $T = 1$ MeV, the average entropy of the whole chain increases, however, dips around magic neutron numbers are still pronounced. Again, we note that calculations with assumed spherical symmetry agree well with axially deformed results up to $N = 42$. In addition to having a spherical shape, pairing effects in calcium isotopes vanish at around $T = 1$ MeV. By further increasing the temperature to $T = 2$ MeV, the entropy curve gets smoother since the temperature is high enough to scatter the nucleons above the closed shells, reducing the dips at magic numbers. This is more pronounced for heavier isotopes, where, due to the neutron excess, nucleons can couple with the continuum more easily. In Fig. 13(b) we display the entropy as a function of neutron number in the chain of Nd isotopes. At $T = 0.5$ MeV temperature, two dips in the entropy curve are visible for magic numbers $N = 82$ and $N = 126$. By increasing the temperature to $T = 1$ MeV, it is interesting to notice large differences in entropy between axially deformed and spherical calculations for midshell nuclei that can be explained by the

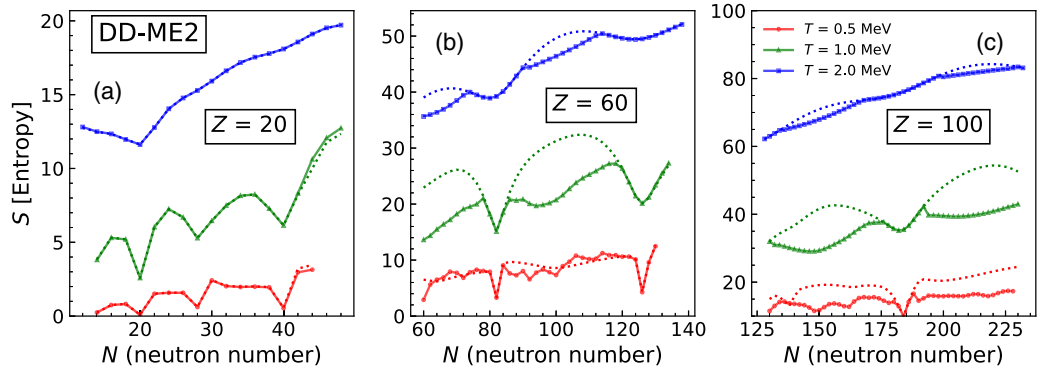

FIG. 13. Entropy S as a function of neutron number for (a) $Z = 20$, (b) $Z = 60$, and (c) $Z = 100$ isotopic chains. The full line denotes the axially deformed calculations while the dotted line represents calculations assuming spherical symmetry. Calculations are performed with the DD-ME2 interaction.

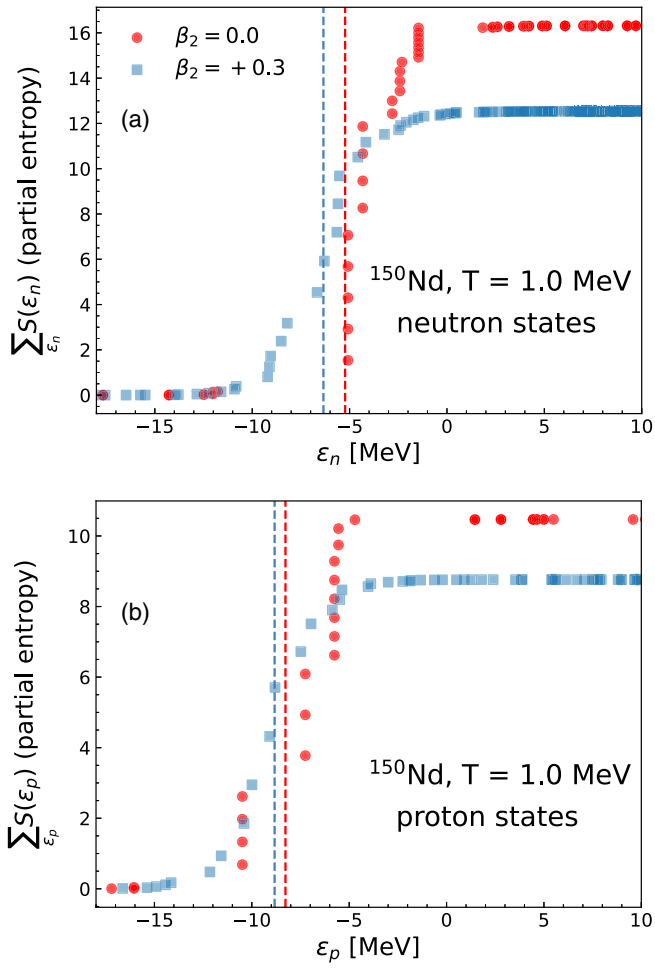

FIG. 14. Cumulative sum of the partial entropy $S(\varepsilon_i)$ of the Nuc + Vap system as a function of the single-particle energy ε_i for (a) neutrons and (b) protons. Calculations are performed for spherical (red circles) and prolate (blue squares) configurations in ^{150}Nd at $T = 1$ MeV with DD-ME2 interaction. Dashed vertical lines denote corresponding Fermi levels for spherical (red) and prolate (blue) configurations.

large prolate deformation of Nd isotopes. Since the deformation effects induce degeneracy splitting between different angular-momentum projections, there are more states among which the occupation is scattered. This leads to a reduction in entropy compared with the simple spherical geometry, where the entropy is maximum at midshell. At $T = 2$ MeV, these differences are still visible, although less pronounced since the deformation splitting of single-particle levels is reduced at higher temperature. To illustrate the origin of differences between the entropy of spherical and axially deformed nuclei, we investigate the changes in entropy when summation in Eq. (21) is performed over different single-particle levels. In particular, we express Eq. (21) as a sum over partial entropy $S(\varepsilon_i)$ up to a certain single-particle level characterized by energy ε_i. As an example nucleus, we select ^{150}Nd at $T = 1$ MeV and perform calculations for spherical ($\beta_2 = 0$) and prolate ($\beta_2 = +0.3$) configurations. Results for the cumulative entropy $\sum_{\varepsilon_i} S(\varepsilon_i)$ of the Nuc + Vap system are shown in Fig. 14(a) for neutron states and in Fig. 14(b) for proton states. As expected, the major contribution to entropy comes from states near the Fermi level. While we observe a smooth increase in entropy around the Fermi level for the deformed configuration, we notice a sharp increase in entropy around the Fermi level for the spherical configuration. In the case of the spherical configuration, it is evident that degenerate states near the Fermi level have a more pronounced impact on increasing entropy compared with the respective prolate configuration. For instance, let us suppose that a spherical level with angular momentum j exists around the Fermi level with occupation close to 0.5. The deformation effects would break this level into $(2j + 1)/2$ levels (assuming time-reversal symmetry), with occupations either slightly above or below 0.5. Consequentially, since the maximum contribution to the entropy stems from levels with occupation 0.5, the entropy for the deformed levels will be lower than for the corresponding spherical levels. For ^{150}Nd, the effect is more pronounced for the neutron states but is significant for the proton states as well. Therefore, deformation tends to depopulate the states in the vicinity of the Fermi level, thus decreasing entropy.

For the fermium chain in Fig. 13(c), the entropy shows a dip around the $N = 184$ magic number. As the temperature is increased to $T = 1$ MeV, there is a region between $N = 176$–192, where the entropy curve follows the spherical calculation, indicating a widening region of spherical shape around the shell closure number with increasing temperature. At $T = 2$ MeV, this region is even wider, $N = 168$–198, with additional two regions displaying spherical shapes around proton and neutron drip-lines. Therefore, we conclude that deformation effects lead to a reduction of entropy compared with simple spherical calculation, confirming that entropy probes microscopic effects within nuclear structure calculations.

Contrary to entropy, the excitation energy, defined as the difference between the total energy of the atomic nucleus at finite and zero temperature $E^* = E(T) - E(T = 0)$, is accessible in the experiments. The nucleus at finite temperature can be conceptualized as an ensemble average over the excited states, weighted by the Boltzmann factors. Therefore, unlike zero-temperature calculations where the mean-field solution yields the ground state, at finite-temperature we have a mixture of excited states represented by excitation energy E^*. In Fig. 15, we show the distribution of the excitation energy E^* across the nuclide map for three functionals: DD-ME2, DD-PC1 and DD-PCX. Calculations are performed at $T = 0.5$, 1, and 2 MeV temperatures. Starting from $T = 0.5$ MeV, we observe that the excitation energy varies rapidly across the nuclide map. The nucleon shell-closure numbers can be recognized as dips in excitation energy. By increasing the temperature to $T = 1$ MeV, the doubly magic nuclei (and nuclei in their vicinity) display smaller values of excitation energy in comparison to deformed isotopes. An interesting phenomenon occurs at $T = 2$ MeV where nuclei with shell-closure have larger excitation energies compared with other midshell nuclei. Indeed, by examining the results for deformed nuclei at $T = 2$ MeV in Fig. 5, their signature is clearly seen in the lower panel of Fig. 15. Once the energy gap of the closed shells has been surmounted by additional energy, spherical nuclei in the vicinity of shell closure are more easily excited compared with the deformed nuclei. This result is in

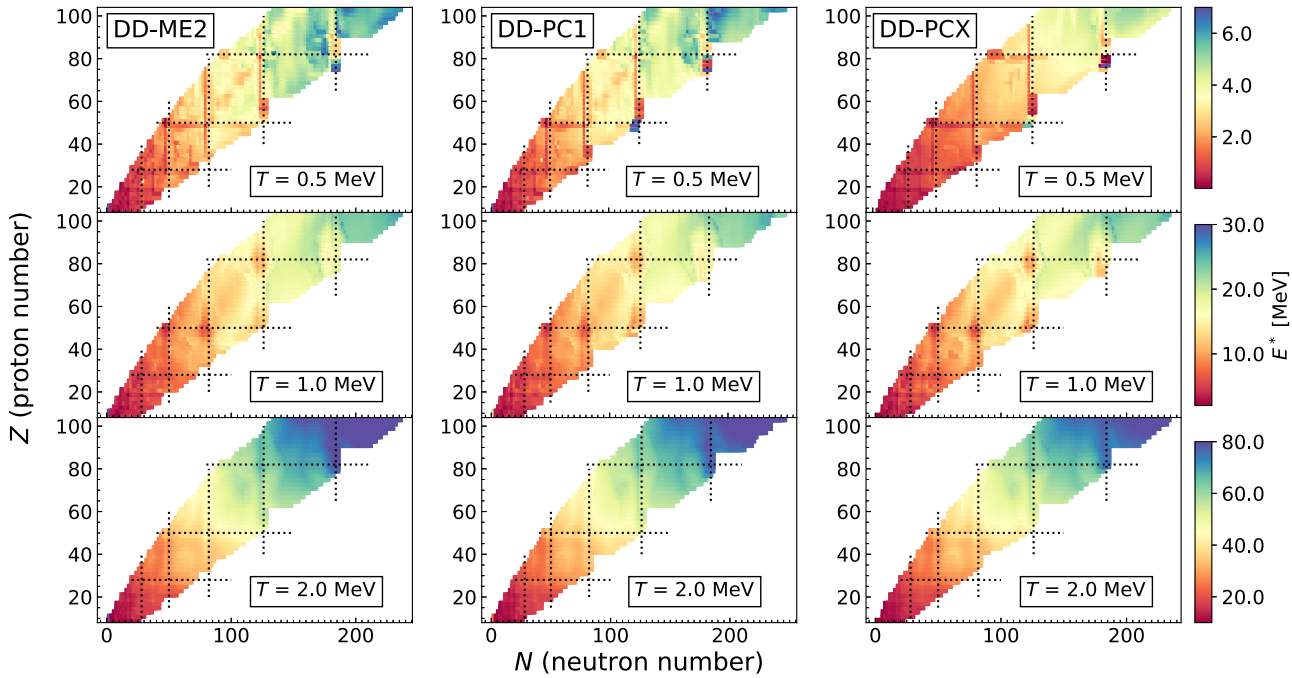

FIG. 15. Distribution of the excitation energy E^* for even-even nuclei with proton number in the range $8 \leqslant Z \leqslant 104$ at temperatures $T = 0.5$, 1.0, and 2.0 MeV. Calculations are performed with DD-ME2 (left panels), DD-PC1 (middle panels), and DD-PCX (right panels) interactions.

agreement with the corresponding nonrelativistic calculation in Ref. [40].

Furthermore, it is interesting to study the temperature dependence of entropy and excitation energy for some selected nuclei. Calculations are performed for the ^{126}Sn isotope with a closed proton shell and the midshell ^{150}Nd isotope. Results are shown in Fig. 16 for temperatures in range $T = 0$–2 MeV and calculations are performed by employing the DD-ME2 functional. First, we notice that both entropy and excitation energy increase with temperature; however, the dependence on temperature is not smooth but rather displays visible kinks. For ^{150}Nd shown in Fig. 16(a), two such kinks are visible, first at $T_c^p \approx 1.1$ MeV and second at $T_c^s \approx 1.4$ MeV. They correspond to the critical temperature of pairing and shape phase transition, respectively. On the other hand, in Fig. 16(b), ^{126}Sn displays only one kink related to the pairing collapse at $T_c^p \approx 0.7$ MeV. This can be understood by taking into account the spherical shape of the ^{126}Sn isotope for all values of temperature due to the proton shell closure.

Once the pairing and shape effects are washed out, nucleus behaves approximately as an idealized Fermi gas. Therefore, entropy should be proportional to temperature $S = 2aT$, while the excitation energy depends quadratically on temperature as $E^* = aT^2$. The constant of proportionality a depends on the density of states as well as the number of nucleons [1,74]. To compare our results with the Fermi gas model, in Fig. 16 we include a fit to temperature dependence of S and E^* for the Fermi gas model. Results of the fit for the parameter a using two different definitions are shown in Table I. Since this model is valid for high temperatures, only temperature values in

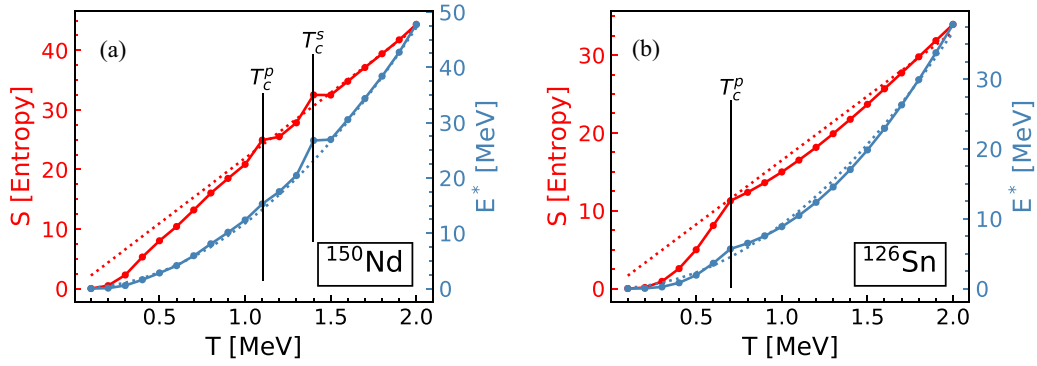

FIG. 16. Entropy S (red line) and excitation energy E^* (blue line) as a function of temperature for (a) ^{150}Nd and (b) ^{126}Sn isotopes. The dotted lines denote the fits of the calculated values of entropy and excitation energy to the expression of the Fermi gas model $S = 2aT$ and $E^* = aT^2$. Only points with $T \geqslant 1.5$ MeV are included in the fit.

TABLE I. Values of constant a obtained by fitting entropy and excitation energy calculated with the DD-ME2 interaction to temperature dependence of S and E^* for the Fermi gas model, i.e., $S = 2aT$ and $E^* = aT^2$. Fit was performed for two isotopes, ^{150}Nd and ^{124}Sn, leading to results that are consistent within 10%.

	$a(^{150}\text{Nd})$ [MeV^{-1}]	$a(^{126}\text{Sn})$ [MeV^{-1}]
$S = 2aT$	10.96 ± 0.04	8.24 ± 0.09
$E^* = aT^2$	11.89 ± 0.02	9.23 ± 0.09

range $T \geqslant 1.5$ MeV were included in the fit. The fitted curves are denoted by the dotted lines in Fig. 16. The fitted values of level-density parameter a, either to entropy or excitation energy, for the same nucleus agree within 10%. We observe that, once $T > T_c$, where $T_c = \max\{T_c^p, T_c^s\}$, both entropy and excitation energy approach the temperature dependence of the Fermi gas model. These results indicate the validity of an independent-nucleon picture at high temperatures, when shell effects are diminished.

Finally, we compare our calculations for the excitation energy with those obtained in Ref. [40]. For a fair comparison, we note that the calculations presented in Ref. [40] assume spherical symmetry. At temperature $T = 1$ MeV [see Figs. 17(a)–17(c)], we observe large differences in midshell nuclei originating from deformation effects, as well as the differences in the functionals included in our calculations. The mechanism of deformation effects in calculating the excitation energies is similar to the one previously discussed in the case of entropy. As the neutron drip line is approached, we notice a significant contribution from the continuum states, as expected. At $T = 2$ MeV [see Figs. 17(d)–17(f)], all nuclei included in the calculations become spherical, leading to more consistent results between the nonrelativistic SkM* and relativistic DD-PCX functionals. For neutron-rich isotopes, we notice the crucial role of the proper continuum subtraction procedure, while for nuclei close to the valley of stability, discrepancies can be attributed to different EDFs. Nevertheless, at $T = 2$ MeV, excitation energies of most nuclei in a given isotopic chain are altered by the continuum contribution. Therefore, for accurate calculation of excitation energies, one has to include treatment of continuum for temperatures $T \approx 2$ MeV for most nuclei and even at lower temperatures for nuclei near the drip-line.

VI. SUMMARY AND OUTLOOK

The finite-temperature relativistic Hartree-Bogoliubov model has been supplemented with the vapor subtraction procedure using the BLV prescription. This approach has been employed to study global bulk properties of even-even $8 \leqslant Z \leqslant 104$ nuclei. The importance of the vapor subtraction in weakly bound nuclei has been analyzed by studying examples of ^{160}Gd and ^{210}Gd isotopes. For ^{210}Gd, without the subtraction procedure, the potential-energy curve at finite temperature depends strongly on the size of the basis used to discretize the FT-RHB equation. By subtracting the contribution of the vapor, results become independent of the basis size.

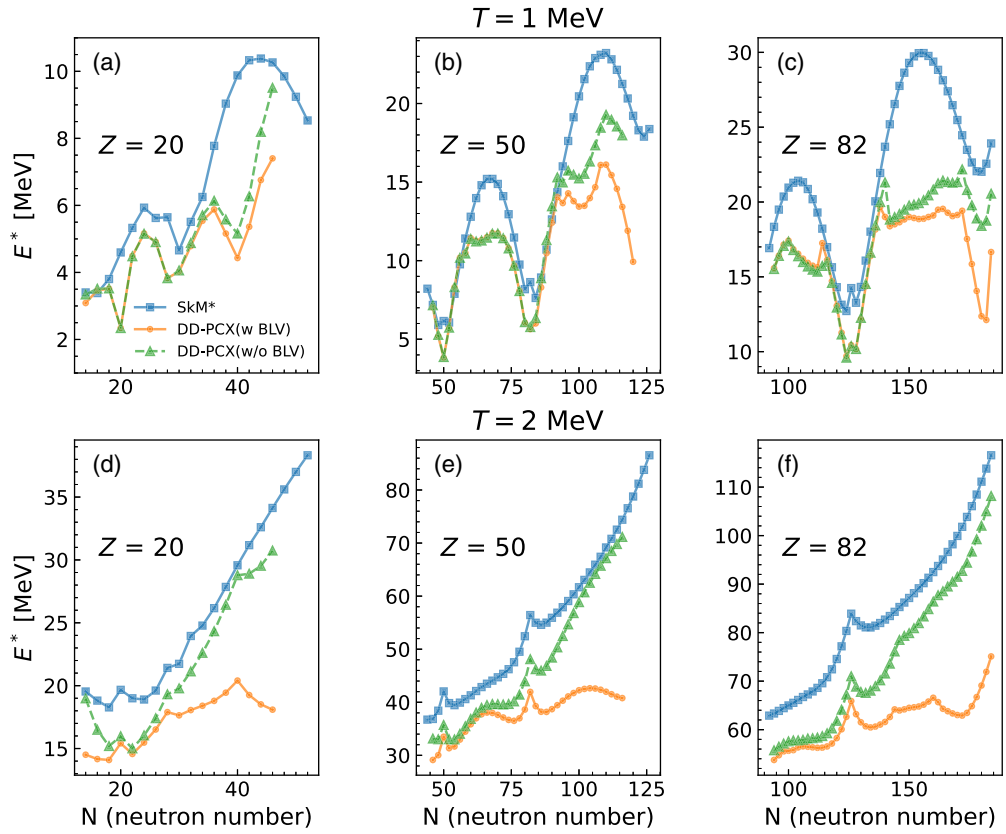

FIG. 17. Same as in Fig. 10 but for excitation energy E^*.

The bulk properties of nuclei with increasing temperature are mainly influenced by (i) decrease of pairing gaps, leading to a transition from a superfluid to a normal state, (ii) a shape-phase transition from an axially deformed to a spherical configuration, and (iii) reduction of shell gaps. The results of this work can be summarized as follows:

(1) The neutron emission lifetimes τ_n decrease abruptly towards the two-neutron drip line. Furthermore, when increasing the temperature, the neutron emission lifetimes are lower and display smoother behavior across the isotopic chains due to the reduction of shell effects.
(2) The isoscalar quadrupole deformations β_2^{IS} show visible changes once the temperature is $T \geqslant 0.5$ MeV. Shape-phase transitions occur initially in nuclei with small deformations and extend towards the midshell nuclei as the temperature increases. At temperature around $T = 2$ MeV, most even-even nuclei are predicted to be spherical.
(3) Neutron-skin thickness ΔR_{np} shows only moderate changes with increasing temperatures. At around $T = 2$ MeV, the isotopic dependence of ΔR_{np} becomes almost linear for nuclei with neutron excess. On the other hand, proton-rich nuclei show a departure from the linear dependence due to the Coulomb interaction.
(4) The pairing gaps are reduced with increasing temperature. The precise temperature of transition between the superfluid and normal phase depends on the strength of the pairing interaction, but for temperatures $T \geqslant 1$ MeV, pairing properties vanish for almost all nuclei, except the lightest ones.
(5) The isotopic dependence of entropy displays a signature of the underlying microscopic structure. Namely, the entropy decreases towards shell-closure numbers and reaches its peak midshell. As the temperature is increased, shell effects are reduced and the isotopic dependence of entropy becomes smooth. In comparison to entropy, excitation energy shows an opposite behavior. Due to the higher density of states in deformed nuclei, their excitation energy is lower as compared with spherical isotopes. Both entropy and excitation energy display kinks near the temperature of the pairing and shape phase transition. At high temperatures, nuclear properties begin to mirror those of an idealized Fermi gas.

Once the continuum is properly treated, one could extend the results to nuclei beyond the drip line. Those nuclei would be characterized by a nonequilibrated emission of particles, but their bulk properties at finite-temperature could still be inferred. Furthermore, calculations in this work do not include odd nuclei. Within the mean-field models, odd nuclei are usually treated within the equal-filling approximation (EFA), however, it remains questionable how to extend the EFA to statistical averages within the FT-RHB. Nevertheless, we leave the consideration of odd nuclei as well as nuclei beyond the two-nucleon drip-line for future work.

ACKNOWLEDGMENTS

We acknowledge helpful discussions with W. Nazarewicz and S. E. Agbemava. This work is supported by the QuantiXLie Centre of Excellence, a project co financed by the Croatian Government and European Union through the European Regional Development Fund, the Competitiveness and Cohesion Operational Programme (KK.01.1.1.01.0004). This work was supported by the U.S. Department of Energy under Award Number DOE-DE-NA0004074 (NNSA, the Stewardship Science Academic Alliances program). A.R. acknowledges support by the US National Science Foundation under Grant PHY-1927130 (AccelNet-WOU: International Research Network for Nuclear Astrophysics [IReNA]). This work was supported in part through computational resources and services provided by the Institute for Cyber-Enabled Research at Michigan State University. E.Y. acknowledges the support from the Science and Technology Facilities Council (UK) through Grant ST/Y000013/1.

[1] A. Bohr and B. Mottelson, *Nuclear Structure (In 2 Volumes)* (World Scientific Publishing Company, 1998), Vol. 1, pp. 434–437.
[2] H.-T. Janka, K. Langanke, A. Marek, G. Martínez-Pinedo, and B. Müller, Phys. Rep. **442**, 38 (2007).
[3] G. Baym, T. Hatsuda, T. Kojo, P. D. Powell, Y. Song, and T. Takatsuka, Rep. Prog. Phys. **81**, 056902 (2018).
[4] D. Jacquet, J. Galin, B. Borderie, D. Gardes, D. Guerreau, M. Lefort, F. Monnet, M. F. Rivet, X. Tarrago, E. Duek, and J. M. Alexander, Phys. Rev. C **32**, 1594 (1985).
[5] N. Herrmann, R. Bock, H. Emling, R. Freifelder, A. Gobbi, E. Grosse, K. D. Hildenbrand, R. Kulessa, T. Matulewicz, F. Rami, R. S. Simon, H. Stelzer, J. Wessels, P. R. Maurenzig, A. Olmi, A. A. Stefanini, W. Kühn, V. Metag, R. Novotny, M. Gnirs *et al.*, Phys. Rev. Lett. **60**, 1630 (1988).
[6] J. Pochodzalla, W. A. Friedman, C. K. Gelbke, W. G. Lynch, M. Maier, D. Ardouin, H. Delagrange, H. Doubre, C. Grégoire, A. Kyanowski, W. Mittig, A. Péghaire, J. Péter, F. Saint-Laurent, Y. P. Viyogi, B. Zwieglinski, G. Bizard, F. Lefèbvres, B. Tamain, and J. Québert, Phys. Rev. Lett. **55**, 177 (1985).
[7] J. Pochodzalla, C. K. Gelbke, W. G. Lynch, M. Maier, D. Ardouin, H. Delagrange, H. Doubre, C. Grégoire, A. Kyanowski, W. Mittig, A. Péghaire, J. Péter, F. Saint-Laurent, B. Zwieglinski, G. Bizard, F. Lefèbvres, B. Tamain, J. Québert, Y. P. Viyogi, W. A. Friedman *et al.*, Phys. Rev. C **35**, 1695 (1987).
[8] O. Wieland, A. Bracco, F. Camera, G. Benzoni, N. Blasi, S. Brambilla, F. Crespi, A. Giussani, S. Leoni, P. Mason, B. Million, A. Moroni, S. Barlini, V. L. Kravchuk, F. Gramegna, A. Lanchais, P. Mastinu, A. Maj, M. Brekiesz, M. Kmiecik *et al.*, Phys. Rev. Lett. **97**, 012501 (2006).
[9] K. A. Snover, Annu. Rev. Nucl. Part. Sci. **36**, 545 (1986).
[10] A. Corsi, O. Wieland, S. Barlini, A. Bracco, F. Camera, V. L. Kravchuk, G. Baiocco, L. Bardelli, G. Benzoni, M. Bini, N. Blasi, S. Brambilla, M. Bruno, G. Casini, M. Ciemala, M.

Cinausero, F. C. L. Crespi, M. D'Agostino, M. Degerlier, A. Giaz *et al.*, Phys. Rev. C **84**, 041304(R) (2011).
[11] J. J. Gaardhøje, Nucl. Phys. A **488**, 261 (1988).
[12] M. Kicińska-Habior, K. Snover, J. Behr, C. Gossett, Y. Alhassid, and N. Whelan, Phys. Lett. B **308**, 225 (1993).
[13] E. Suraud, M. Pi, and P. Schuck, Nucl. Phys. A **492**, 294 (1989).
[14] H. A. Bethe, Rev. Mod. Phys. **9**, 69 (1937).
[15] P. Bonche, S. Koonin, and J. W. Negele, Phys. Rev. C **13**, 1226 (1976).
[16] C. Simenel and A. Umar, Prog. Part. Nucl. Phys. **103**, 19 (2018).
[17] E. Suraud, Nucl. Phys. A **462**, 109 (1987).
[18] S. Levit and P. Bonche, Nucl. Phys. A **437**, 426 (1985).
[19] X. Y. Qu and Y. Zhang, Phys. Rev. C **99**, 014314 (2019).
[20] T. T. Sun, S. Q. Zhang, Y. Zhang, J. N. Hu, and J. Meng, Phys. Rev. C **90**, 054321 (2014).
[21] J. C. Pei, A. T. Kruppa, and W. Nazarewicz, Phys. Rev. C **84**, 024311 (2011).
[22] P. Bonche, S. Levit, and D. Vautherin, Nucl. Phys. A **436**, 265 (1985).
[23] P. Bonche, S. Levit, and D. Vautherin, Nucl. Phys. A **427**, 278 (1984).
[24] T. Vertse, A. T. Kruppa, and W. Nazarewicz, Phys. Rev. C **61**, 064317 (2000).
[25] A. L. Goodman, Nucl. Phys. A **352**, 30 (1981).
[26] A. L. Goodman, Nucl. Phys. A **352**, 45 (1981).
[27] A. L. Goodman, Phys. Rev. C **34**, 1942 (1986).
[28] J. Egido, P. Ring, and H. Mang, Nucl. Phys. A **451**, 77 (1986).
[29] J. Erler, N. Birge, M. Kortelainen, W. Nazarewicz, E. Olsen, A. M. Perhac, and M. Stoitsov, Nature (London) **486**, 509 (2012).
[30] S. Goriely, S. Hilaire, M. Girod, and S. Péru, Phys. Rev. Lett. **102**, 242501 (2009).
[31] J. P. Delaroche, M. Girod, J. Libert, H. Goutte, S. Hilaire, S. Péru, N. Pillet, and G. F. Bertsch, Phys. Rev. C **81**, 014303 (2010).
[32] E. Yüksel, E. Khan, K. Bozkurt, and G. Colò, Eur. Phys. J. A **50**, 160 (2014).
[33] Y. F. Niu, Z. M. Niu, N. Paar, D. Vretenar, G. H. Wang, J. S. Bai, and J. Meng, Phys. Rev. C **88**, 034308 (2013).
[34] J. J. Li, J. Margueron, W. H. Long, and N. Van Giai, Phys. Rev. C **92**, 014302 (2015).
[35] N. Schunck, D. Duke, and H. Carr, Phys. Rev. C **91**, 034327 (2015).
[36] Y. Zhu and J. C. Pei, Phys. Rev. C **94**, 024329 (2016).
[37] E. Yüksel, F. Mercier, J.-P. Ebran, and E. Khan, Phys. Rev. C **106**, 054309 (2022).
[38] Y. Zhu and J. C. Pei, Phys. Rev. C **90**, 054316 (2014).
[39] R. Lisboa, M. Malheiro, and B. Carlson, Nucl. Phys. B, Proc. Suppl. **199**, 345 (2010).
[40] E. Yüksel, Nucl. Phys. A **1014**, 122238 (2021).
[41] D. Vretenar, A. Afanasjev, G. Lalazissis, and P. Ring, Phys. Rep. **409**, 101 (2005).
[42] T. Nikšić, D. Vretenar, and P. Ring, Prog. Part. Nucl. Phys. **66**, 519 (2011).
[43] G. A. Lalazissis, T. Nikšić, D. Vretenar, and P. Ring, Phys. Rev. C **71**, 024312 (2005).
[44] T. Nikšić, D. Vretenar, and P. Ring, Phys. Rev. C **78**, 034318 (2008).
[45] A. Afanasjev, S. Agbemava, D. Ray, and P. Ring, Phys. Lett. B **726**, 680 (2013).
[46] S. E. Agbemava, A. V. Afanasjev, D. Ray, and P. Ring, Phys. Rev. C **89**, 054320 (2014).
[47] K. Zhang, M.-K. Cheoun, Y.-B. Choi, P. S. Chong, J. Dong, Z. Dong, X. Du, L. Geng, E. Ha, X.-T. He, C. Heo, M. C. Ho, E. J. In, S. Kim, Y. Kim, C.-H. Lee, J. Lee, H. Li, Z. Li, T. Luo *et al.*, At. Data Nucl. Data Tables **144**, 101488 (2022).
[48] M. Belabbas, J. J. Li, and J. Margueron, Phys. Rev. C **96**, 024304 (2017).
[49] B. K. Agrawal, T. Sil, J. N. De, and S. K. Samaddar, Phys. Rev. C **62**, 044307 (2000).
[50] W. Zhang and Y. F. Niu, Phys. Rev. C **97**, 054302 (2018).
[51] W. Zhang and Y. F. Niu, Phys. Rev. C **96**, 054308 (2017).
[52] R. Lisboa, M. Malheiro, and B. V. Carlson, Phys. Rev. C **93**, 024321 (2016).
[53] A. Ravlić, E. Yüksel, T. Nikšić, and N. Paar, Nat. Commun. **14**, 4834 (2023).
[54] E. Yüksel, T. Marketin, and N. Paar, Phys. Rev. C **99**, 034318 (2019).
[55] A. N. Antonov, D. N. Kadrev, M. K. Gaidarov, P. Sarriguren, and E. M. de Guerra, Phys. Rev. C **95**, 024314 (2017).
[56] T. Nikšić, N. Paar, D. Vretenar, and P. Ring, Comput. Phys. Commun. **185**, 1808 (2014).
[57] P. Ring, L. Robledo, J. Egido, and M. Faber, Nucl. Phys. A **419**, 261 (1984).
[58] T. Nikšić, D. Vretenar, P. Finelli, and P. Ring, Phys. Rev. C **66**, 024306 (2002).
[59] Y. Tian, Z.-Y. Ma, and P. Ring, Phys. Rev. C **80**, 024313 (2009).
[60] J. L. Egido, Phys. Rev. Lett. **61**, 767 (1988).
[61] J. L. Egido and P. Ring, J. Phys. G **19**, 1 (1993).
[62] A. L. Goodman, Phys. Rev. C **29**, 1887 (1984).
[63] V. Martin, J. L. Egido, and L. M. Robledo, Phys. Rev. C **68**, 034327 (2003).
[64] J. Dobaczewski, W. Nazarewicz, T. R. Werner, J. F. Berger, C. R. Chinn, and J. Dechargé, Phys. Rev. C **53**, 2809 (1996).
[65] P. Bonche, S. Levit, and D. Vautherin, Nucl. Phys. A **428**, 95 (1984).
[66] J. Besprosvany and S. Levit, Phys. Lett. B **217**, 1 (1989).
[67] J. L. Egido, L. M. Robledo, and V. Martin, Phys. Rev. Lett. **85**, 26 (2000).
[68] M. Brack and P. Quentin, Phys. Lett. B **52**, 159 (1974).
[69] S. Levit and Y. Alhassid, Nucl. Phys. A **413**, 439 (1984).
[70] L.-W. Chen, C. M. Ko, and B.-A. Li, Phys. Rev. C **72**, 064309 (2005).
[71] M. Centelles, X. Roca-Maza, X. Viñas, and M. Warda, Phys. Rev. Lett. **102**, 122502 (2009).
[72] X. Roca-Maza and N. Paar, Prog. Part. Nucl. Phys. **101**, 96 (2018).
[73] J. N. De and S. K. Samaddar, Phys. Rev. C **85**, 024310 (2012).
[74] H. A. Bethe, Phys. Rev. **50**, 332 (1936).